J. Fluid Mech. (1993), *vol.* 255, *pp.* 373–409

Nonlinear dynamics of capillary bridges: theory

By TAY-YUAN CHEN AND JOHN TSAMOPOULOS†
Department of Chemical Engineering, State University of New York at Buffalo, Buffalo, NY 14260, USA

(Received 26 April 1992 and in revised form 23 March 1993)

Finite-amplitude, forced and free oscillations of capillary bridges are studied. They are characterized by a resonant frequency and a damping rate which, in turn, depend on fluid properties, dimensions of the bridge, gravitational force relative to surface tension and amplitude of the external disturbance. The Navier–Stokes equations are solved numerically using the Galerkin/finite-element methodology for discretization in space and implicit finite differences with adaptive time stepping for discretization in time. It is found that the resonant frequency decreases and the damping rate increases almost linearly with the oscillation amplitude. Their relative changes from their corresponding values at infinitesimal amplitude depend on fluid properties and dimensions of the bridge. Moreover, careful measurement of the resonant frequency and damping rate in a well-controlled experiment may provide quite accurate values for properties of the liquid over a wide range of modified Reynolds numbers.

1. Introduction

Studies on the stability and dynamics of fluid bridges between two solid objects date back to the classic experiments by Plateau (1863) and the theories by Young (1805), Laplace (1805), and Rayleigh (1879). Current interest has increased since fluid bridges arise in quite diverse, natural and industrial operations. Such operations include particulates agglomeration (Chen, Tsamopoulos & Good 1991), flow, evaporation, and condensation in porous media (Melrose 1966; Zasadzinski *et al.* 1987), materials processing on Earth or in a microgravity environment (Preisser, Schwabe & Scharmann 1983; Brown 1988; Duranceau & Brown 1986, 1988).

Here the nonlinear dynamics of isothermal liquid bridges will be studied. Mason (1970) first observed that it was possible to establish standing waves on the surface of a liquid bridge by vibrating its support and adjusting its length. Similar experiments were performed by Fowle, Wang & Strong (1979) who also developed a theory under the assumption that the motion is of small amplitude, the fluid inviscid and the flow irrotational. Subsequently, Meseguer (1983), Rivas & Meseguer (1984) and Sanz (1985), among others, studied the dynamics of axisymmetric bridges. These authors employed either a one-dimensional Cosserat model or restricted the analysis to inviscid fluids.

More recently, Borkar & Tsamopoulos (1991) used a boundary-layer analysis for fluids with large but finite Reynolds number in order to satisfy both the no-penetration and no-slip boundary conditions at solid/liquid interfaces. Oscillation frequencies and damping rates were calculated for bridges undergoing small-amplitude oscillations. Damping could be due to either the viscous boundary layers or the restrained motion of the three-phase contact line. Moreover, Tsamopoulos, Chen & Borkar (1992) determined the range of validity of this analysis by performing linear calculations for

† Author to whom correspondence should be addressed.

arbitrary Reynolds number Re and generalized their results by including the gravitational force and three-dimensional disturbances. Such a complete linear analysis had not been performed previously since analytic solutions turned out to be quite complicated and required verification and extension by numerical ones. Results covered a wide range of modified Re, $2 < Re < 1000$, which includes materials with high viscosity and low surface tension, e.g. ethylene glycol or molten ceramics, and vice versa, e.g. water or liquid metals. Thus, it was shown that the boundary-layer theory is valid for about $Re > 100$.

One of the goals of our studies is to examine the possibility and explore the conditions under which forced and free oscillations of liquid bridges can be used to measure surface tension and viscosity of various materials including molten ceramics and semiconductors. Quite often in such cases, fluids are at high temperatures, require minimum contact with the testing apparatus and cover a wide range of viscosities. For a short review on this subject see Tsamopoulos *et al.* (1992). As it was discussed there, either static bridge shapes or their resonance frequencies may be related to the surface tension of the material. In addition, either resonance frequencies or damping rates of free oscillations may be related to the material viscosity. This method seemed to be most promising for materials with modified Reynolds number less than 100, depending on bridge geometry and the mode being excited. In a quite different context, oscillations of the supporting rods may decrease concentration or temperature inhomogeneities by inducing convective transport throughout the bridge.

Clearly, it is very important to assess the effect of inertia forces and other nonlinearities during oscillations since they are inevitably present in most experiments performed by us and others. It is well known that inertia decreases resonance frequencies, at least for fluids with low viscosity; see, for example, Tsamopoulos & Brown (1983, 1984). Therefore, it may alter resonance frequencies even when $Re < 100$. It is also likely that inertia will affect damping rates predicted by linear theory. Furthermore, the significant deviation between the damping rates predicted by the boundary layer and viscous theories for $10 < Re < 100$ might be attributed to the fact that viscous dissipation may take place not only on the solid/liquid interfaces but also on the gas/liquid interfaces and in the bulk of the liquid. Clearly, then, the former theory would be inapplicable and even more so any theory that assumes inviscid fluids and irrotational flow. The present analysis clarifies this point further.

Here calculations of the shape of a liquid bridge and fluid flow inside it are carried out. The bridge is subject to large-amplitude, forced oscillations which are induced by vertical vibrations of the upper bounding wall. By varying the forcing frequency for a given bridge geometry and fluid properties, resonance is identified when the bridge surface deviates furthest from a cylindrical shape. Thus, the nonlinear resonance frequency is computed. Knowledge of the linear eigenfrequency (Tsamopoulos *et al.* 1992) proved most useful in organizing and interpreting the results presented here and in keeping to a reasonable limit the number of calculations required, which were quite expensive. Subsequently, motion of the upper wall is interrupted and the nonlinear damping rate is determined.

In all cases, the bridge shape at every time step is determined by the interplay of pressure, viscous forces and surface tension and it is calculated simultaneously with the other variables. All interfaces are described relative to a cylindrical coordinate system in a fashion similar to that employed by Poslinski & Tsamopoulos (1991). The dynamics are governed by the Navier–Stokes equations subject to kinematic and dynamic boundary conditions on the moving surfaces. Gravitational effects are included and their relative importance is measured by the gravitational Bond number.

Governing equations and boundary conditions are given in §2. The Galerkin/finite-element solution methodology as adopted for the present problem is summarized in §3. Results are presented and discussed in §4 and conclusions are drawn in §5.

2. Governing equations

A liquid bridge of volume $\bar{V}_b$ is considered. As shown in figure 1, the bridge is situated between two solid and coaxial rods of equal radius $\bar{R}$. The bottom rod is stationary and the top rod is undergoing a sinusoidal vertical oscillation according to $\bar{z} = \bar{L} + \bar{A}\sin(\bar{\omega}\bar{t})$, where $\bar{A}$ is the amplitude, $\bar{\omega}$ is the forcing frequency of oscillation, and overbars indicate dimensional quantities. The liquid wets the two planar solid surfaces which initially are at a distance $\bar{L}$ from each other and forms a fixed and circular contact line on the edge of each rod, irrespective of the state of motion of the bridge. $\bar{L}$ is kept below the Rayleigh stability limit in a gravity-free case ($\bar{L} \leqslant 2\pi\bar{R}$), or below the corresponding limit point when gravity is present; see Tsamopoulos, Poslinski & Ryan (1988). It should be pointed out that these limiting values of $\bar{L}$ for stable shapes have been calculated and are relevant for static bridges only. It is also assumed that the surrounding gas has negligible density and viscosity so that it does not affect the dynamics of the liquid bridge. Furthermore, bulk properties of the liquid (density ρ, and viscosity μ) as well as surface tension γ, are uniform and constant under the present isothermal analysis.

Oscillatory disturbances initiate motion of the liquid, which can be easily detected at the free surface of the bridge. This motion is affected by the physical properties of the liquid, its static shape which in turn depends on $\bar{R}$, $\bar{L}$, and gravity, and the amplitude and frequency of oscillation. Gravity acts downwards along the z-axis. The usual cylindrical coordinate system (r, θ, z) with origin at the bottom rod and coaxial with the axis of symmetry between the two rods is defined. The corresponding components of velocity are $\bar{V} = (\bar{u}, \bar{v}, \bar{w})$. The goal is to compute the time-dependent flow field, the nonlinear resonant frequency and damping rate of the system. All these will be related to the physical properties of the liquid, bridge geometry, and the amplitude of the motion.

Conservation equations of mass and momentum are written in dimensionless form:

$$\nabla \cdot V = 0, \tag{2.1}$$

$$\sigma^2 Re\left(\frac{\partial V}{\partial t} + \alpha V \cdot \nabla V\right) = -Re\,\nabla \cdot (PI) + \sigma \nabla \cdot \tau, \tag{2.2}$$

where the modified pressure is defined by $P = (p + Bz)/\alpha$, I is the identity tensor, and the extra stress is defined by $\tau = (\nabla V + \nabla V^T)$. Variables have been rendered dimensionless with respect to their dimensional counterparts as follows:

$$z = \frac{\bar{z}}{\bar{L}}, \quad r = \frac{\bar{r}}{\bar{R}}, \quad p = \bar{p}\frac{\bar{R}}{\gamma}, \quad \bar{V} = \frac{\bar{V}}{\bar{A}\bar{\omega}}, \quad t = \bar{t}\bar{\omega}.$$

As a result, the gravitational Bond number $B = \rho g \bar{R}\bar{L}/\gamma$ (g is the gravitational acceleration), the forcing amplitude $\alpha = \bar{A}/\bar{R}$, the forcing frequency $\sigma = \bar{\omega}(\rho\bar{R}^3/\gamma)^{\frac{1}{2}}$, and the modified Reynolds number, $Re = (\rho\gamma\bar{R})^{\frac{1}{2}}/\mu$ arise in (2.2). This scaling has been preferred for this problem since it groups together all relevant fluid properties in the modified Re which is also the only available dimensionless number in the linear problem (Tsamopoulos *et al.* 1992). The same dimensionless group is sometimes

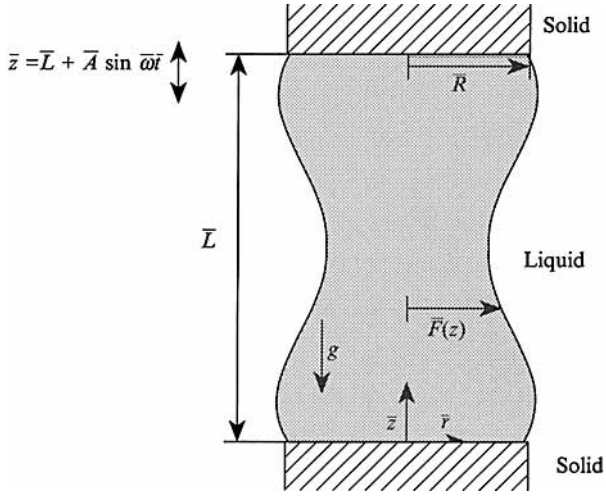

FIGURE 1. Schematic representation of a liquid bridge.

referred to as the Suratman number, $Su = \rho\gamma\bar{R}/\mu^2$, or the Ohnesorge number, $Oh = \mu/(\rho\gamma\bar{R})^{\frac{1}{2}}$. When α is very small the convective term in (2.2) drops out and the linearized Navier–Stokes equation results. Different lengthscales have been used in the radial and axial directions and their ratio, $\Lambda = \bar{R}/\bar{L}$, is the so-called aspect ratio and serves as the fifth parameter of this system. It arises, for example, in the dimensionless form of the gradient operator:

$$\nabla = \boldsymbol{e}_r \frac{\partial}{\partial r} + \boldsymbol{e}_\theta \frac{1}{r}\frac{\partial}{\partial \theta} + \boldsymbol{e}_z \Lambda \frac{\partial}{\partial z}. \tag{2.3}$$

Since only axisymmetric disturbances and motion are examined ($\partial/\partial\theta = 0$), the azimuthal velocity is zero throughout the bridge ($v = 0$) and

$$u = \frac{\partial w}{\partial r} = 0 \quad \text{at} \quad r = 0. \tag{2.4}$$

Moreover, the usual no-slip boundary conditions are applied at both solid surfaces which, for forced oscillations, are

$$u = 0 \quad \text{at} \quad z = 0 \quad \text{and} \quad z = 1 + G(t) \equiv 1 + \alpha\Lambda \sin t. \tag{2.5}$$

The no-penetration boundary condition is imposed at the surface of the bottom rod and the normal velocity of the fluid in contact with the upper boundary surface follows the oscillation of the rod,

$$w = 0 \quad \text{at} \quad z = 0, \tag{2.6a}$$

$$w = \cos t \quad \text{at} \quad z = 1 + G(t). \tag{2.6b}$$

Furthermore, at the liquid/gas interface, the tangential stress must be zero and the total normal stress must be balanced by the capillary force:

$$\boldsymbol{t}_z \boldsymbol{N} : \boldsymbol{\tau} = 0, \quad r = f(z, t), \tag{2.7}$$

$$[Re(-p - Bz)\boldsymbol{I} + \alpha\sigma\boldsymbol{\tau}] : \boldsymbol{NN} + Re\, 2\mathscr{H} = 0, \quad r = f(z, t). \tag{2.8}$$

In (2.7) and (2.8), the ambient pressure has been taken as the reference pressure and $\boldsymbol{t}_z$ and $\boldsymbol{N}$ are the unit tangent and outward pointing normal to the interface,

respectively. In the Mongé representation, a point on the axisymmetric interface can be described by the position vector $\boldsymbol{F}(z,t) = f(z,t)\,\boldsymbol{e}_r + z\boldsymbol{e}_z$. Consequently, $\boldsymbol{N}$ and $\boldsymbol{t}_z$ are given by

$$\boldsymbol{N} = \frac{\boldsymbol{e}_r - \Lambda f_z \boldsymbol{e}_z}{(1+\Lambda^2 f_z^2)^{\frac{1}{2}}}, \tag{2.9}$$

$$\boldsymbol{t}_z = \frac{\Lambda f_z \boldsymbol{e}_r + \boldsymbol{e}_z}{(1+\Lambda^2 f_z^2)^{\frac{1}{2}}}, \tag{2.10}$$

where the subscript z denotes partial differentiation with respect to the z-coordinate. The curvature of the axisymmetric interface, $\mathscr{H}$, has been scaled by $\bar{R}^{-1}$ and is equal to

$$2\mathscr{H} = \frac{1}{f}\left[(1+\Lambda^2 f_z^2)^{\frac{1}{2}} - \Lambda^2 \frac{\partial}{\partial z}\frac{f f_z}{(1+\Lambda^2 f_z^2)^{\frac{1}{2}}}\right], \tag{2.11}$$

with respect to the cylindrical coordinate system. The final boundary condition that arises at the moving interface is the kinematic condition. It is used to determine the unknown location of the moving interface and it equates the velocity of the surface to the fluid velocity there

$$\boldsymbol{N}\cdot\frac{\partial \boldsymbol{F}}{\partial t} = \alpha \boldsymbol{N}\cdot\boldsymbol{V}, \quad r = f(z,t). \tag{2.12}$$

Throughout the motion, the contact line of the liquid/gas interface with each cylindrical rod remains fixed at the edge of each rod (Benjamin & Scott 1979),

$$f(z,t) = 1 \quad \text{at} \quad z = 0 \quad \text{and} \quad z = 1+G(t). \tag{2.13}$$

In addition, the volume of the liquid bridge must remain constant. In the present analysis, it is taken to be equal to the volume of the space between the rods before the external excitation is applied on the liquid bridge,

$$V_b \equiv \frac{\bar{V}_b}{\pi \bar{R}^2 \bar{L}} = \int_0^{1+G(t)} f^2\,\mathrm{d}z = 1. \tag{2.14}$$

Equation (2.14) serves as an *a posteriori* check of the accuracy of the present calculations. Transient integration is initiated from the rest state, $V = 0$. In the case of zero gravity ($B = 0$), the rest state is $f(z,0) = 1$, and $p = 1$. If the gravitational force is included ($B \neq 0$), the rest state must be calculated by solving (2.8) and (2.14) for $f(z,0)$ and the hydrostatic pressure p; see Tsamopoulos *et al.* (1992). The necessary modification of boundary conditions (2.5), (2.6) and (2.13) during free oscillations will be discussed later.

3. Numerical solution technique

Conservation equations along with boundary and initial conditions are solved using the Galerkin/finite-element method. The procedure employed here has evolved from the studies by Ettouney & Brown (1983) and Duranceau & Brown (1986) for steady-state problems and by Derby & Brown (1986) and Poslinski & Tsamopoulos (1991) for non-steady-state ones. The central idea is to map the moving and unknown boundaries onto a fixed domain using a non-orthogonal coordinate transformation. As an alternative, Kistler & Scriven (1983) and Kheshgi & Scriven (1984), parametrized the physical domain by introducing spines.

The relevant non-orthogonal mapping is described in §3.1 and the finite-element discretization in §3.2. Fully implicit time integration is carried out with special attention on the time steps at start up and at reversal in the direction of motion of the upper rod. This is explained in §3.3. The modified Newton iterative procedure for solving the final algebraic set of equations and certain accuracy tests are given in §3.4.

3.1. *Non-orthogonal transformation*

For transient free-surface motion, the position and shape of the meniscus is not only unknown in space but also evolves in time. In order to take into account changes in the flow domain, the equations that result from the finite-element discretization are transformed from the original coordinate system (r, z, t) to a fixed computational coordinate system (η, ξ, τ) by the following mapping:

$$\eta = r/f(z,t), \tag{3.1}$$

$$\xi = z/[1+G(t)], \tag{3.2}$$

$$\tau = t. \tag{3.3}$$

Equations (3.1)–(3.3) map the deformed meniscus back to a fixed cylindrical domain defined in $(0 \leqslant \xi \leqslant 1,\ 0 \leqslant \eta \leqslant 1)$. Consequently, the finite-element mesh is generated on this computational domain and remains the same throughout the transient integration. Thus, the difficulty of updating the deforming elements in the physical domain is avoided. However, the complexity of this formulation increases owing to introduction of new spatial and time derivatives into the governing equations; see Derby & Brown (1986), and Poslinski & Tsamopoulos (1991). Derivatives in the physical domain are transformed into derivatives in the computational domain according to

$$\frac{\partial(\,)}{\partial r} = \frac{\partial(\,)}{\partial \eta}\left(\frac{\partial r}{\partial \eta}\right)^{-1}, \tag{3.4}$$

$$\frac{\partial(\,)}{\partial z} = \frac{\partial(\,)}{\partial \xi}\left(\frac{\partial z}{\partial \xi}\right)^{-1} - \frac{\partial(\,)}{\partial \eta}\left(\frac{\partial r}{\partial \xi}\right)\left(\frac{\partial r}{\partial \eta}\right)^{-1}\left(\frac{\partial z}{\partial \xi}\right)^{-1}, \tag{3.5}$$

$$\frac{\partial(\,)}{\partial t} = \frac{\partial(\,)}{\partial \tau} - \frac{\partial(\,)}{\partial \xi}\frac{\partial z}{\partial \tau}\left(\frac{\partial z}{\partial \xi}\right)^{-1} + \frac{\partial(\,)}{\partial \eta}\left[\frac{\partial r}{\partial \xi}\frac{\partial z}{\partial \tau} - \frac{\partial r}{\partial \tau}\frac{\partial z}{\partial \xi}\right]\left(\frac{\partial r}{\partial \eta}\right)^{-1}\left(\frac{\partial z}{\partial \xi}\right)^{-1}. \tag{3.6}$$

The terms $\partial r/\partial \tau$, $\partial z/\partial \tau$, $\partial r/\partial \xi$, $\partial r/\partial \eta$, and $\partial z/\partial \xi$ are obtained from the inverse mapping of (3.1)–(3.3), and introduce the location of the unknown interfaces explicitly into the formulation. Since the position of a material point depends on the location of the moving free surface and the position of the oscillating top rod, these derivatives are functions of time through the inverse mapping of (3.1) and (3.2). As a result, the second term on the right-hand side of (3.6) is due to axial motion of the physical domain. Also, the third term in (3.6) is more complicated than that obtained by Poslinski & Tsamopoulos (1991), because the length in the z-direction is fixed in their study, whereas here the bounding interfaces in both the r- and z-directions are in motion. Therefore, this term is composed of both radial, $\partial r/\partial \tau$, and axial, $\partial z/\partial \tau$, motion of the physical domain.

3.2. *Finite-element discretization*

The computational domain $(0 \leqslant \eta \leqslant 1,\ 0 \leqslant \xi \leqslant 1)$ is partitioned into a finite-element mesh using isoparametric rectangular elements. The location of the gas/liquid interface and the velocity field are represented by Lagrangian quadratic $\chi_i(\xi)$ and biquadratic

$\phi_i(\eta, \xi)$ basis functions, respectively, and the pressure field is approximated by bilinear basis functions $\psi_i(\eta, \xi)$ (i.e. the mixed interpolation for the primitive variables, velocities and pressure, is used). The finite-element representations are written as

$$V(\eta, \xi, \tau) = \sum_{i=1}^{M} V_i(\tau)\,\phi_i(\eta, \xi), \tag{3.7}$$

$$P(\eta, \xi, \tau) = \sum_{i=1}^{N} P_i(\tau)\,\psi_i(\eta, \xi), \tag{3.8}$$

$$f(\xi, \tau) = \sum_{i=1}^{L} f_i(\tau)\,\chi_i(\xi), \tag{3.9}$$

where L, M, and N are the number of coefficients in each expansion and V_i, P_i, and f_i are the nodal values of the corresponding variables. Owing to axisymmetry, V is composed of the radial and axial velocity components only. The residual equations are constructed using Galerkin's principle. Equations (2.1), (2.2) and (2.13) are multiplied by the trial functions ψ_i, ϕ_i and χ_i, respectively, and they are integrated over the domain. The second-order derivatives in the momentum equations are reduced to first-order ones by applying the divergence theorem, and the resulting boundary integrals are directly evaluated by the appropriate boundary conditions ((2.7) and (2.8)). Hence, the weak form of the governing equations written first in the physical domain is as follows:

$$R_{Ci} = \int_{\Omega} \psi_i\, \nabla \cdot V \,\mathrm{d}\Omega, \tag{3.10}$$

$$R_{Mi} = \int_{\Omega} \phi_i \left[\sigma^2 Re\left(\frac{\partial V}{\partial t} + \alpha V \cdot \nabla V\right) + \frac{1}{\mathrm{r}}\left(-\frac{Re}{\alpha} P + \sigma \tau_{\theta\theta}\right) e_r\right] \mathrm{d}\Omega + \int_{\Omega} \nabla \phi_i \cdot (-Re\, P I + \sigma \tau)\,\mathrm{d}\Omega + \int_{S} \phi_i \frac{Re}{\alpha} 2\mathscr{H} N \,\mathrm{d}S, \tag{3.11}$$

$$R_{ki} = \int_{0}^{1+G(t)} \chi_i \left(\frac{1}{\alpha}\frac{\partial f}{\partial t} - u + \Lambda f_z w\right) \mathrm{d}z. \tag{3.12}$$

The residual equations, $R \equiv [R_{Ci}\, R_{Mi}\, R_{ki}]^T = 0$, corresponding to continuity, momentum, and kinematic equations and will be used to calculate the vector of unknowns $\beta = [P_i,\ V_i,\ f_i]$, respectively. In these general expressions $\mathrm{d}\Omega \equiv r\,\mathrm{d}r\,\mathrm{d}z$ denotes the differential area with $0 \leqslant r \leqslant f(z, t)$ and $0 \leqslant z \leqslant 1 + G(t)$, whereas $\mathrm{d}S \equiv (1 + \Lambda^2 f_z^2)^{\frac{1}{2}}\,\mathrm{d}z$ denotes differential arclength along the surface. The mean curvature of the free surface arises in the boundary integral on the right-hand-side of (3.11). Next, the procedure described by Keunings (1986) is employed in order to reduce the second-order derivatives in $2\mathscr{H}$ to first-order ones. By doing so Lagrangian basis functions may still be used for representing $f(z, t)$. The main idea is that the mean curvature must be decomposed into two terms

$$2\mathscr{H} N = -\Lambda \frac{\mathrm{d}t_z}{\mathrm{d}S} + \frac{1}{R_2} N, \tag{3.13}$$

where t_z, N and $\mathrm{d}S$ were defined earlier. Moreover, R_2 represents the second principal radius of curvature and is given by

$$R_2 = f(1 + \Lambda^2 f_z^2)^{\frac{1}{2}}. \tag{3.14}$$

Using (3.13) and (3.14) and integrating by parts the boundary integral term in (3.11) yields

$$\int_S \phi_i 2\mathscr{H} N \mathrm{d}S = \int_0^{1+G} \left[\phi_i (1+\Lambda^2 f_z^2)^{\frac{1}{2}} + \frac{\Lambda^2 (\partial \phi_i/\partial z) f f_z}{(1+\Lambda^2 f_z^2)^{\frac{1}{2}}}\right] \mathrm{d}z\, \boldsymbol{e}_r + \int_0^{1+G} \frac{\Lambda f (\partial \phi_i/\partial z)}{(1+\Lambda^2 f_z^2)^{\frac{1}{2}}} \mathrm{d}z\, \boldsymbol{e}_z. \tag{3.15}$$

In (3.15) the essential condition for the interface ($f = 1$ at $z = 0$ and at $z = 1+G(t)$) has been employed. Finally, (3.10)–(3.12) and (3.15) are transformed to the fixed computational domain by the mapping given in the previous section. As a result, the shape function for the free surface and the motion of the top rod appear explicitly throughout the equation set, and the limits of integration become constant. The resulting equations in their final form are too long to be given here, and can be found in Chen (1991). Evaluation of integrals is performed by Gaussian quadrature rules defined on an isoparametric rectangular element. Nine Gauss points are used for two-dimensional integrals and three Gaussian points are used for one-dimensional integrals.

3.3. *Transient integration*

The residual equations (3.10)–(3.12) comprise a set of algebraic equations and first-order differential equations with respect to time. Schematically they may be written as

$$\boldsymbol{M}(\boldsymbol{\beta}) \frac{\partial \boldsymbol{\beta}}{\partial \tau} = \boldsymbol{Q}(\boldsymbol{\beta}), \tag{3.16}$$

where $\boldsymbol{Q}(\boldsymbol{\beta})$ is composed of those terms in the residual vectors that do not involve derivatives with respect to time and $\boldsymbol{M}(\boldsymbol{\beta})$ is the mass matrix. $\boldsymbol{M}(\boldsymbol{\beta})$ is singular because time derivatives do not appear in the residuals formed from the continuity equation. Therefore, only implicit integration schemes may be used. The time derivatives, $\partial V/\partial \tau$ and $\partial f/\partial \tau$, that arise in the momentum and kinematic residuals are approximated with finite differences. To this end, either an explicit Euler predictor–backward Euler corrector, or a second-order Adams–Bashforth predictor–trapezoid rule corrector are employed. The predictor–corrector scheme automatically adjusts the time-step size so as to keep the time truncation error below a predefined tolerance level, which in this study is set at 10^{-4}. For further details see Gresho, Lee & Sani (1980), Kheshgi & Scriven (1984) and Poslinski & Tsamopoulos (1991). Here only the required modifications to this scheme will be briefly discussed.

During the initial transients of the motion and in order to suppress any numerical oscillations in the exceedingly small values of the dependent variables, calculations are started with four backward Euler steps of equal size. This size is chosen as $\Delta\tau = 10^{-2}$ in order to accomplish an optimum balance between numerical error and computational cost. Whenever a new timestep is selected, the code verifies first that the upper rod has not reversed its motion during this time step, otherwise $\Delta\tau$ is decreased accordingly. When the upper rod reaches either a maximum or a minimum in its oscillatory path (at $\tau = 2n\pi + \frac{1}{2}\pi$ or $\tau = 2n\pi + \frac{3}{2}\pi$), two backward Euler steps of equal size, 10^{-2}, are used. This is necessary because now the previous flow field cannot provide a 'good enough' initial guess. Otherwise, the second-order Adams–Bashforth predictor and trapezoid rule corrector is used.

For stable bridges in forced oscillation, integration in time is carried out at least till the induced oscillatory motion of the fluid repeats itself with the same period as that of the rod. It is convenient to represent fluid motion by a measure of deformation of the gas/liquid interface which is also easier to observe experimentally. This deformation

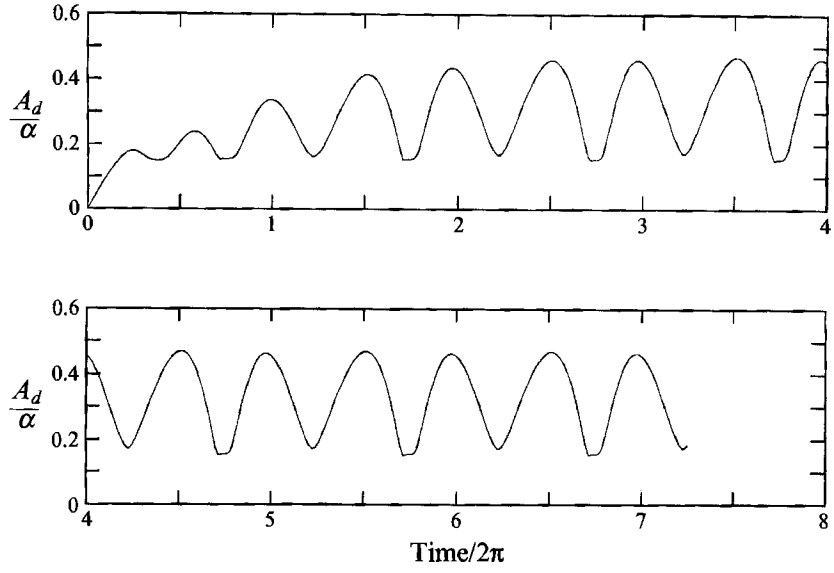

FIGURE 2. Evolution of interface amplitude for a liquid bridge oscillating at resonance in the first mode, with $Re = 10$, $\Lambda = 1/\pi$, $\sigma = 1.25$, and $\alpha = 0.2$.

measure, A_d, is defined as the integral over the bridge length of the absolute value of the deviation of the interface from a cylindrical one,

$$A_d \equiv \int_0^{1+G(t)} |f-1|\,dz. \tag{3.17}$$

The steady oscillatory motion is identified by checking that values of A_d at $\tau = 2n\pi + \frac{1}{2}\pi$, π, $\frac{3}{2}\pi$ and 2π have converged to at least four significant digits between two consecutive cycles. The initial transient damps out in a time interval that depends on the problem parameters. For example, six oscillation cycles are required if $Re = 10$, $\alpha = 0.2$ and $\Lambda = 1/\pi$, whereas eleven oscillation cycles are required if $Re = 20$, $\alpha = 0.2$ and $\Lambda = 1/\pi$, see figures 2 and 3. Given the definition in (3.17) each oscillation cycle is composed of two maxima and two minima. Two consecutive maxima or minima are not identical to each other when the oscillation amplitude is finite, because the motion is not symmetric with respect to the $z = 1$ position. Time integration is terminated when both the steady oscillatory motion has been achieved and the top rod has returned to its initial position. Given the problem parameters, this procedure is repeated under different forcing frequencies. Comparing the maximum values of A_d for different forcing frequencies but the same fluid properties, bridge geometry and oscillation amplitude yields the resonance frequency.

In calculating the damping rate, time integration is started from the steady oscillatory solution at resonance conditions but with the top rod fixed after it reaches its initial position, $z = 1$. Thereafter, $G(t)$ is set to zero in all boundary conditions and other equations where it appears. Four Euler backward steps with equal time-step size, $\Delta\tau = 10^{-2}$, are used to accommodate the step change in axial velocity at the upper rod/fluid interface from $w = \cos(\tau)$ to $w = 0$. Beyond this initial transient, a second-order Adams–Bashforth predictor–trapezoid rule corrector is invoked to complete the time integration. In this case, time integration is stopped when A_d approaches zero for $B = 0$, or returns to its known static value for $B \neq 0$. This is verified in a manner similar to that in forced oscillations.

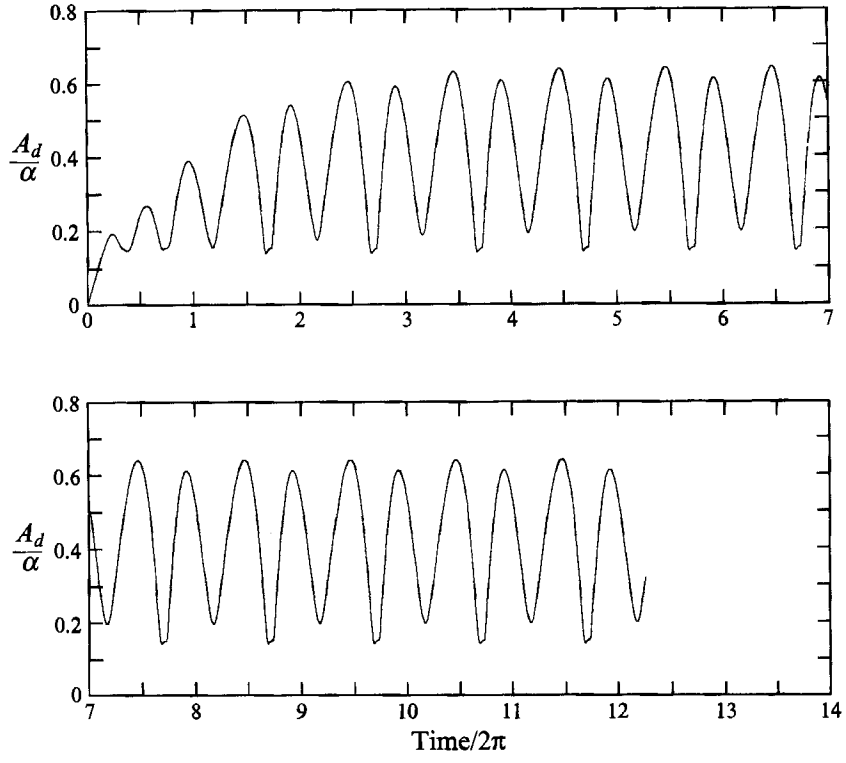

FIGURE 3. As figure 2 but with $Re = 20$, $\sigma = 1.15$.

3.4. *Modified-Newton method and accuracy of calculations*

The ordinary differential equations (3.10)–(3.12) include several nonlinear terms such as the convective term in the momentum equations and the deformation of physical domain introduced by (3.4)–(3.6). At every time step, this nonlinear system of equations is solved iteratively at the corrector step, with the initial guess provided by the predictor. Equation (3.16) is taken as the overall residual equation and Newton–Raphson iterations may be used for updating the unknown vector $\boldsymbol{\beta}$ at the $(n+1)$th iteration,

$$\boldsymbol{\beta}^{(n+1)} = \boldsymbol{\beta}^{(n)} - (\boldsymbol{J}^{(n)})^{-1}\boldsymbol{R}^{(n)}. \tag{3.18}$$

The Jacobian matrix $\boldsymbol{J}$ is computed in closed form by differentiating each term in residual equations (3.10)–(3.12) with respect to the unknown vector.

The most time-consuming procedure in solving this nonlinear system is the inversion of the Jacobian matrix, $\boldsymbol{J}$. This procedure is expedited considerably by updating the Jacobian matrix only when convergence becomes less than linear. This is the so-called modified-Newtonian method. Quite often in the present study, it was necessary to formulate and LU-decompose the Jacobian only once per time step. It was also found that almost quadratic convergence was still attained. The LU-factorization of the Jacobian is accomplished using the ARROW routine (Thomas & Brown 1987). This routine is most efficient if the matrix retains its original form, i.e. if pivoting is avoided. However, essential boundary conditions are imposed on $z = 0$ and $z = 1 + G(t)$ for u and w, and pressure is calculated from the continuity residual. Therefore, straightforward inversion of $\boldsymbol{J}$ would require pivoting. This drawback is circumvented by

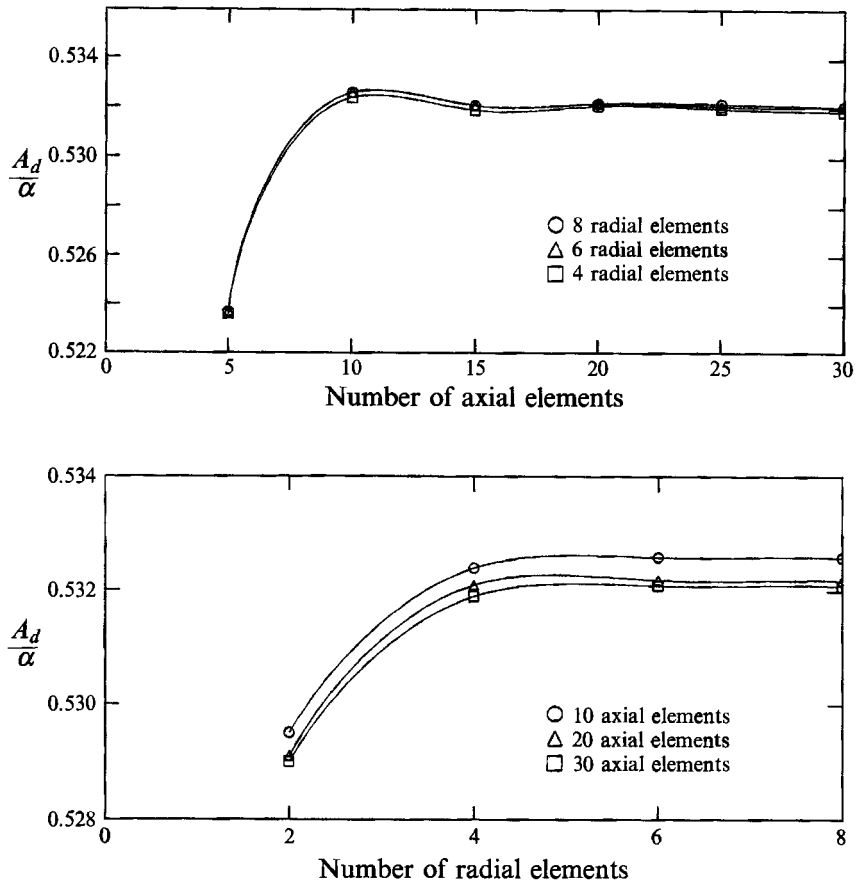

FIGURE 4. Convergence of interface shape with varying number of axial and radial elements, for $Re = 20$, $A = 1/\pi$, $\sigma = 1.15$, and $\alpha = 0.2$.

rearranging both the Jacobian and the residual vector. To this end, the pressure equations of the nodes along $z = 0$ are exchanged with the axial velocity equations on the nodes along $z = \Delta z$, so that they are the first to be assembled.

The converged solution is given in terms of the velocity and pressure fields and the location of the interface. Convergence of the corrector step is measured in terms of the Euclidean norm of the difference between solution vectors in consecutive iterations. It is achieved when $\|\Delta\boldsymbol{\beta}\| < \epsilon_0$, where ϵ_0 is a prespecified tolerance set at 10^{-6} in the present work. Typically, three to four modified-Newton iteration steps are needed to achieve the desired accuracy.

The accuracy of the numerical simulation depends on the mesh structure, and the error arising from time integration. The accuracy due to the spatial discretization is tested by mesh refinement. Figure 4 shows convergence of the calculations in terms of A_d when the top rod returns to $z = 1$ and during steady oscillations. This figure verifies that in calculations with $Re \leqslant 20$, a mesh with only 6 radial and 20 axial equally spaced elements is sufficient in order to achieve at least three accurate digits in calculating deformations in the free surface of the bridge. The same accuracy is achieved in calculating the velocity field. For $30 \leqslant Re \leqslant 50$, 8 radial and 30 axial elements were required in order to capture the larger deformation of the gas/liquid interface. When internal layers appear and at $Re > 30$ the accuracy in the pressure field dropped to only

Mesh	Number of eqs.	IBM 3090-600J	IBM 3084
8 × 20	1624	8000 s	60000 s
8 × 30	2414	12000 s	100000 s

TABLE 1. CPU time for calculating ten oscillation periods when $Re = 30$, $B = 0$, $\alpha = 0.2$ and $A = 1/\pi$ with two different mesh sizes

two digits. Unequally spaced elements did not improve the accuracy of the computations. The mesh employed in the present analysis is finer than the ones employed by Duranceau & Brown (1986, 1988) and Harriott & Brown (1984) in similar problems.

For $Re > 50$ even more axial elements were required in order to resolve the oscillating boundary layers at the solid/liquid interfaces (Borkar & Tsamopoulos 1991). Furthermore, the deformations of the capillary bridge increase considerably and occur faster as the Reynolds number increases. This forces the adaptive time-stepping routine to decrease the time step considerably (250–300 time steps were required for each period at $Re = 50$ as opposed to 120 steps at $Re = 20$). In addition, the lower fluid viscosity takes longer to damp out the initial transients and steady oscillations were achieved only after 20 periods of oscillation. All these effects made such calculations even more expensive.

In the time integration procedure, the size of the time step is controlled and automatically adjusted by the procedure outlined earlier and so that the difference between the predictor and the corrector is smaller than 10^{-4}. The accuracy of time integration is monitored by comparing the instantaneous volume of the liquid bridge calculated by (2.14) with the initial volume of a perfect cylinder, $\bar{V}_b = \pi \bar{R}^2 \bar{L}$. Typically, the variation of volume is less than 0.01 % throughout the calculations. Computations were performed either on the IBM 3090-600J supercomputer at Cornell University or on the IBM 3084 at the University of Buffalo. Table 1 shows the two discretizations used for most calculations, the corresponding number of unknowns and typical computation times.

4. Results and discussion

In the earlier analysis of viscous bridges, Tsamopoulos *et al.* (1992) calculated frequencies and damping rates for infinitesimal disturbances. They solved the relevant generalized eigenvalue problem and reported eigenvalues for the first four eigenmodes. These results comprise an indispensable guide for the present calculations which are considerably more time consuming. Although linear analysis was performed for $2 \leqslant Re \leqslant 1000$, it was found that useful information for physical properties could be extracted at $Re < 100$, where the dependence on Re was easier to detect. This, coupled with the fact that nonlinear calculations become quite expensive as Re increases, restricts the present nonlinear analysis to $Re \leqslant 50$. In addition, excitations of only the first mode are studied here since they are easier to reproduce experimentally and they are the ones that lead to bridge breakup. The nonlinear features of higher modes should be quite similar. In fact, according to the linear analysis, exciting the second mode may be a better way to determine viscosity and surface tension of materials with $70 \leqslant Re \leqslant 200$.

Nonlinear resonance frequencies are calculated in §4.1 as a function of physical

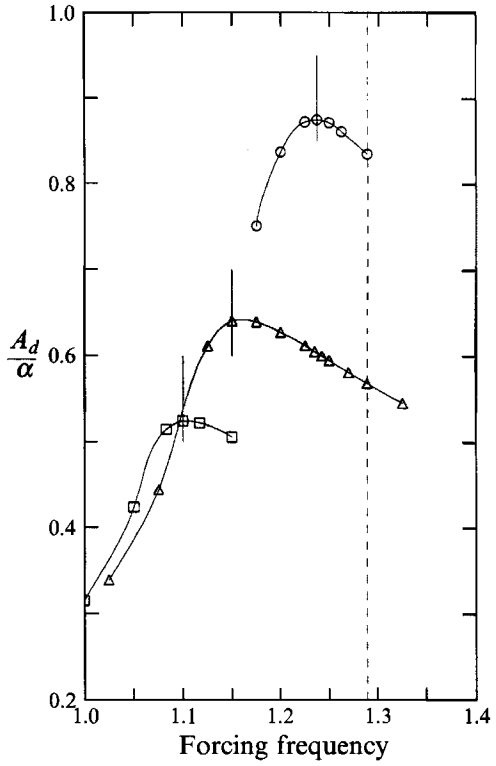

FIGURE 5. Shift of resonant frequency due to increasing forcing amplitude: $\alpha = 0.1$ (○), $\alpha = 0.2$ (△), and $\alpha = 0.3$ (□), with $Re = 20$, $\Lambda = 1/\pi$. Vertical solid lines indicate the resonant frequencies. The vertical dashed line indicates the linear eigenfrequency calculated by Tsamopoulos *et al.* (1992).

properties of the fluid, bridge geometry and amplitude of motion of the upper rod. In §4.2 damping rates are calculated as a function of the same parameters. The total force applied on the lower rod may be measured experimentally to provide additional useful information about the liquid in the bridge. This is explained in §4.3. Gravitational effects are discussed in §4.4.

4.1. *Nonlinear resonance frequency*

According to linear analysis the eigenfrequency should be independent of the amplitude of the disturbance. Nevertheless, we have observed experimentally (Mollot *et al.* 1993) that changes in the forcing amplitude modify the resonating frequency. This has been theoretically shown for oscillating drops with low enough viscosity by carrying out a weakly nonlinear analysis (Tsamopoulos & Brown 1983, 1984).

In order to identify nonlinear resonance conditions of liquid bridges, dynamic simulations are carried out for a given disturbance amplitude and forcing frequency of the top rod. When initial transients dissipate and a steady oscillatory response in the fluid is established the maximum value of A_d (normalized by α) in a complete period is recorded. Subsequently, the forcing frequency is changed, keeping the same amplitude, and finally even the amplitude is changed. Each such repetition produces a single mark in figure 5 and similar figures thereafter. Three separate curves with very distinct maxima, i.e. frequencies at resonance, are shown in figure 5 for three different amplitudes. It may be readily observed that given a liquid with $Re = 20$ and a bridge geometry with $\Lambda = 1/\pi$, increasing the disturbance amplitude reduces the frequency at

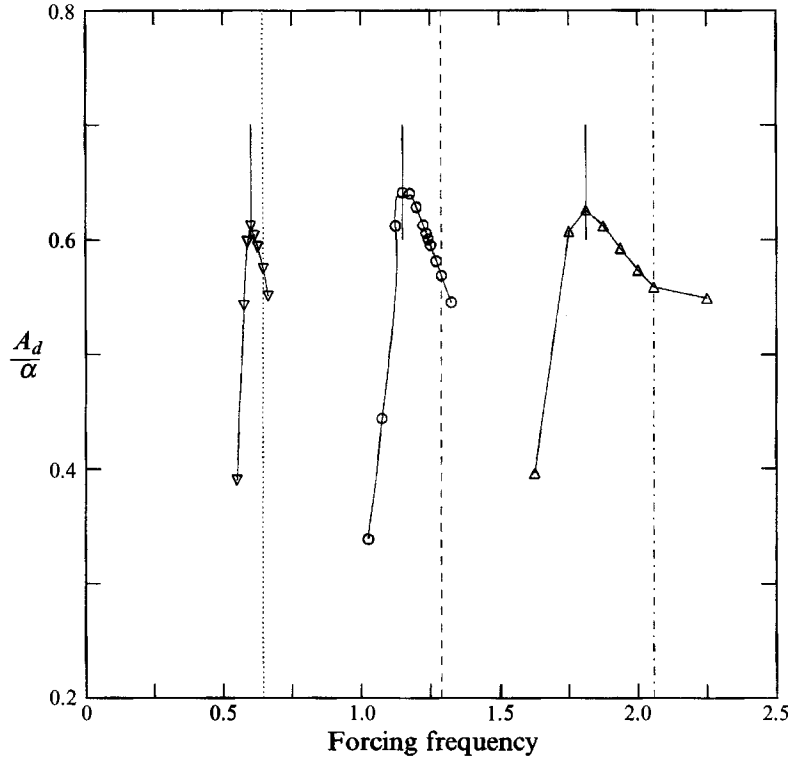

FIGURE 6. Shift of resonant frequency for different aspect ratios: $\Lambda = 0.75/\pi$ (∇, nonlinear or $\cdots$, linear analysis); $\Lambda = 1/\pi$ ($\bigcirc$, nonlinear or ——, linear analysis); and $\Lambda = 1.25/\pi$ ($\triangle$, nonlinear or —·—·—, linear analysis), for $Re = 20$, $\alpha = 0.2$. Vertical solid lines indicate the resonant frequencies. The other vertical lines indicate the corresponding linear eigenfrequencies.

α	Re	$\Lambda\pi$	Linear frequency	Nonlinear frequency	Percentage change
Infinitesimal	20	1	1.289	—	—
0.1	20	1	—	1.2375	−4.0
0.2	20	1	—	1.15	−10.8
0.3	20	1	—	1.10	−14.7
Infinitesimal	20	0.75	0.6445	—	—
0.2	20	0.75	—	0.6125	−5.0
Infinitesimal	20	1.25	2.058	—	—
0.2	20	1.25	—	1.8125	−11.9
Infinitesimal	10	1	1.2733	—	—
0.2	10	1	—	1.25	−1.8
Infinitesimal	30	1	1.2938	—	—
0.2	30	1	—	1.117	−13.7
Infinitesimal	50	1	1.2976	—	—
0.2	50	1	—	1.07	−17.5

TABLE 2. Effect of forcing amplitude, α; fluid properties, Re; and bridge geometry, Λ, on frequency of the liquid bridge at resonance

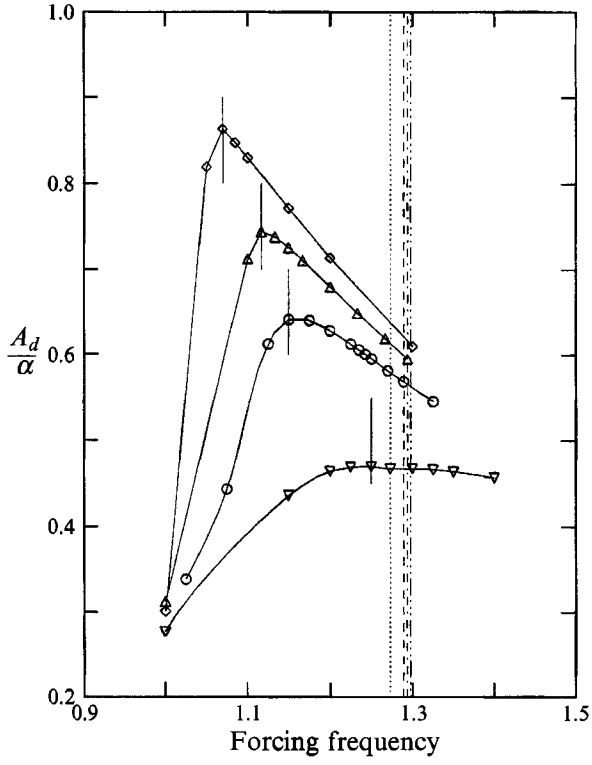

FIGURE 7. Shift of resonant frequency for different Reynolds numbers: $Re = 10$ (∇, nonlinear or ···, linear analysis); $Re = 20$ (○, nonlinear or ———, linear analysis); $Re = 30$ ($\triangle$, nonlinear or —·—·—, linear analysis); and $Re = 50$ ($\diamond$, nonlinear or —···—, linear analysis); with $\Lambda = 1/\pi$ and $\alpha = 0.2$. Vertical solid lines indicate the resonant frequencies. The discontinuous vertical lines indicate the corresponding linear eigenfrequencies.

resonance. The linear frequency is indicated by the vertical discontinuous line in figure 5. It is known that resonance frequencies of liquid drops with high enough Re decrease with the square of the disturbance amplitude (Tsamopoulos & Brown 1983). Here, however, where viscous effects are quite significant and the solid/liquid interfaces provide additional resistance to motion the dependence seems to be a little above linear for $\alpha < 0.2$ and below linear for $\alpha > 0.2$ (see table 2). Similar effects have been obtained by Basaran (1992) for an oscillating viscous drop. The decrease in resonance frequency with increasing α is due to the increases in fluid inertia that the latter causes (see (2.2)). Clearly, prior knowledge of linear frequencies and the expected variation of frequency at resonance assisted in these calculations.

Similar decreases in frequency should be expected for different values of Λ and they are shown in figure 6. It may be readily observed from this figure and table 2 that longer bridges but with same radii yield smaller values of and smaller decreases in resonance frequencies. The former is a linear effect and it should have been expected since in longer bridges the free-surface area is increased and this allows for less restrained motion of the fluid. The latter is a nonlinear effect and it may appear somewhat unexpected since longer bridges should have larger inertia which should lead to larger decreases in resonance frequency. However, it should be noted that the forcing amplitude has been dimensionalized with the rod radius and not the bridge length. Therefore, in spite of keeping the same value of α in figure 6, the real disturbance

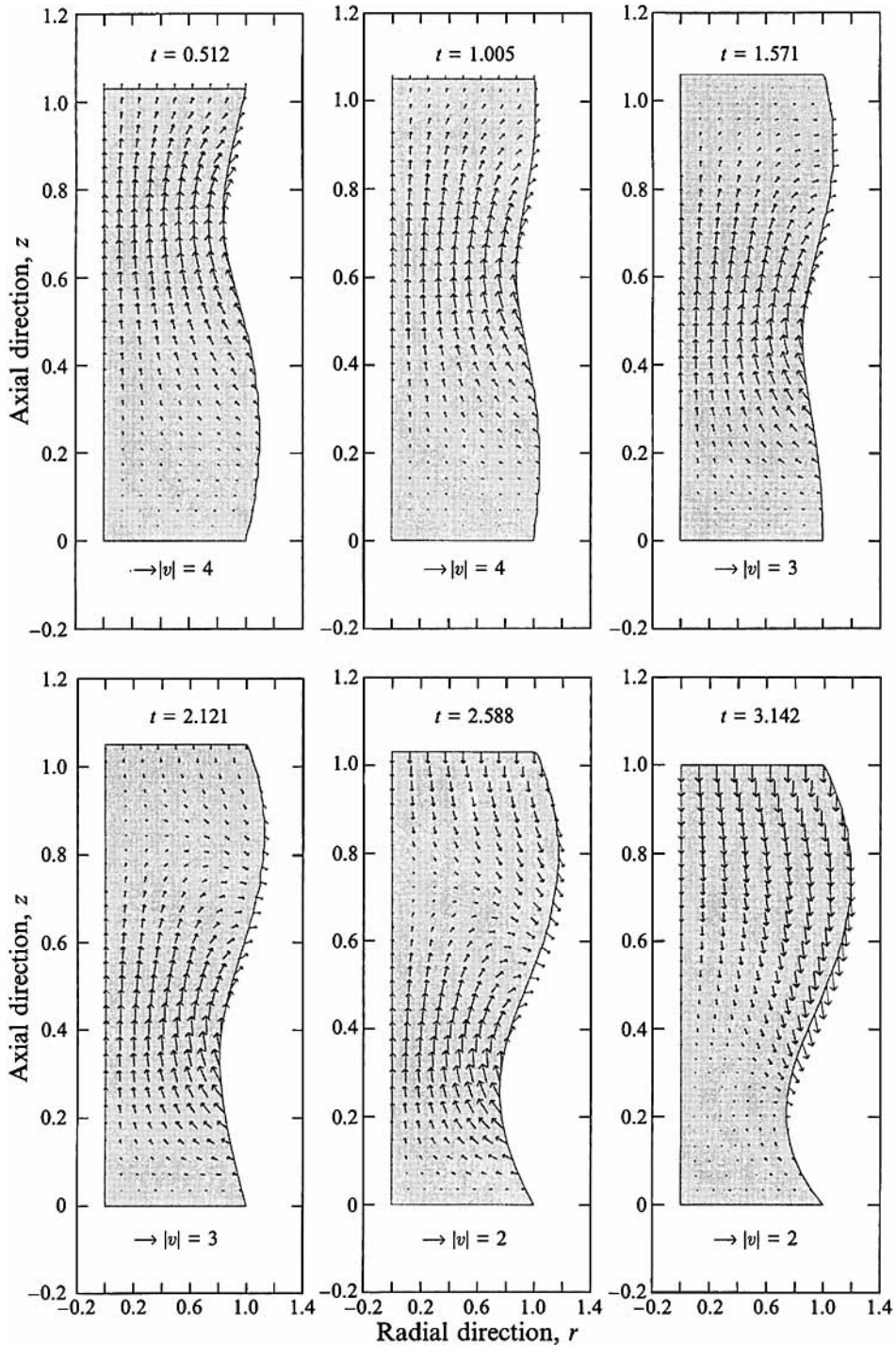

FIGURE 8. For caption see facing page.

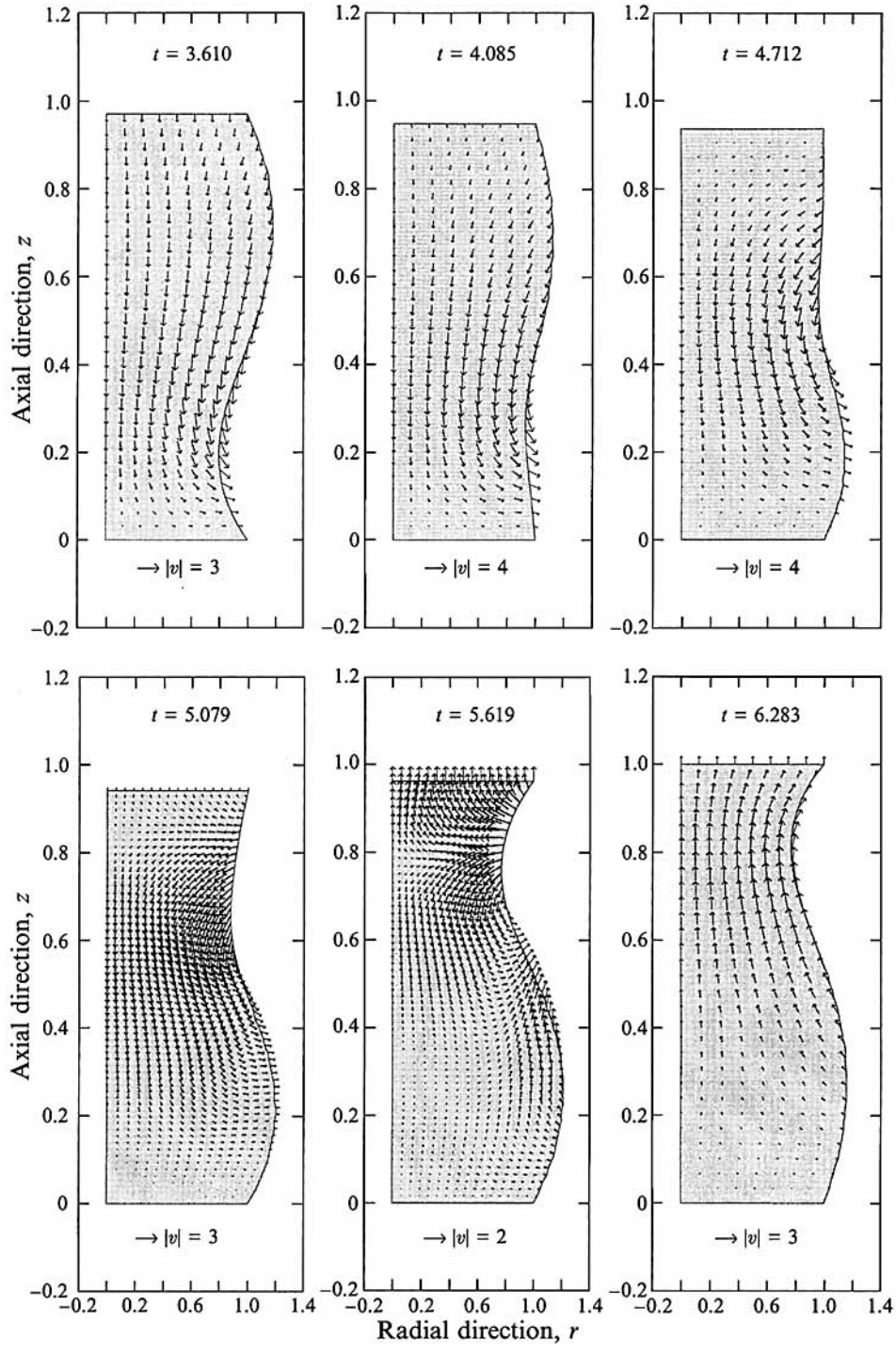

FIGURE 8. Velocity field of an oscillating liquid bridge at resonant frequency of first mode during a particular period ($0 \leqslant t \leqslant 2\pi$), and after initial transients have dissipated with $Re = 30$, $\Lambda = 1/\pi$, $\alpha = 0.2$, and $\sigma = 1.117$.

introduced in the bridge decreases as its length increases or A decreases. If this is taken into account and the percentage in frequency decrease is linearly adjusted to reflect the same amplitude to length ratio, it turns out that the frequency decrease has approximately the same value for $A = 1/\pi$ and $A = 1.25/\pi$. The adjusted value of frequency decrease is still somewhat lower for $A = 0.75/\pi$. This may be attributed to the fact that the frequency decrease does not vary linearly with amplitude.

Next, the effect of Re was studied. Figure 7 shows the results of nonlinear calculations in comparison with linear frequencies. Predictions of linear theory exhibited a relatively small increase in frequency as Re increased and approached the asymptotic value calculated using boundary-layer analysis (Borkar & Tsamopoulos 1991). For example, at $A = 2/\pi = 0.637$ the frequency increased from 3.81 at $Re = 2.5$, to 4.859 at $Re = 10$ and to 5.036 at $Re = 50$. This can also be observed from figure 7 and table 2 where linear results at $A = 1/\pi$ are given. It should be noted that the present definition of A is a factor of π smaller than the one in Borkar & Tsamopoulos (1991) and Tsamopoulos *et al.* (1992).

In contrast to this, nonlinear calculations show that not only is the dependence of the resonant frequency on Re inverted, but also that their values are significantly differentiated from each other for different Reynolds numbers. The decrease in frequency with increased inertia (finite α) turns out to be much more significant than its increase due to decreased viscosity. In general, there are two competing effects. Viscosity retards fluid motion and thereby increases the oscillation period. This is a linear effect. At the same time, viscosity dissipates energy and decreases the oscillation amplitude leading to a decrease in oscillation period. This is a nonlinear effect. Moreover, resonance of different modes can be detected more easily at larger Re, since the maxima at resonance are sharper and further apart when dissipation is smaller. This additional differentiation for different fluids may be used to deduce both surface tension and viscosity from forced oscillation experiments only. In contrast to this, eigenfrequencies for different modes and for $Re < 10$ are quite close together and resonance of each one is more difficult to identify.

The velocity field through a complete period of oscillation in a bridge with $Re = 30$, $A = 1/\pi$ and $\alpha = 0.2$ is shown in figure 8. The forcing frequency has been set at the nonlinear resonance value, $\sigma = 1.117$, and a steady oscillatory motion has been achieved already. Only half of a bridge cross-section along the axis of symmetry is shown for better clarity. Although the characteristic scales are such that the dimensionless bridge radius and height are equal to 1 their dimensional ratio, $1/\pi$, has been preserved in these plots. A measure of the magnitude of velocity in the flow field and at time intervals of $\frac{1}{6}\pi$ (approximately) is also indicated. The velocity vectors are shown at one half of the locations in which they are calculated for clarity, except for cases with stronger recirculation where they are shown at all the calculated points. The oscillatory motion of the upper solid/liquid interface is shown as well.

At this moderate value of Re, the upward motion of the rod propagates first to the fluid nearest to it and causes a smaller motion in the fluid closer to the bottom stationary surface. Fluid near the upper (lower) solid surface also moves away from (towards) the centreline. The highest velocity occurs first closer to the top rod. Later at about $t = \frac{1}{2}\pi$, when the velocity of the top rod is zero, the maximum velocity occurs at around the mid-plane of the bridge. This out-of-phase motion between the oscillating rod and the fluid in the middle of the bridge exists because the timescale for vorticity transport is different from the timescale of oscillation of the rod. This phase lag should be observable if, for example, the force on the lower rod were measured, see §4.3.

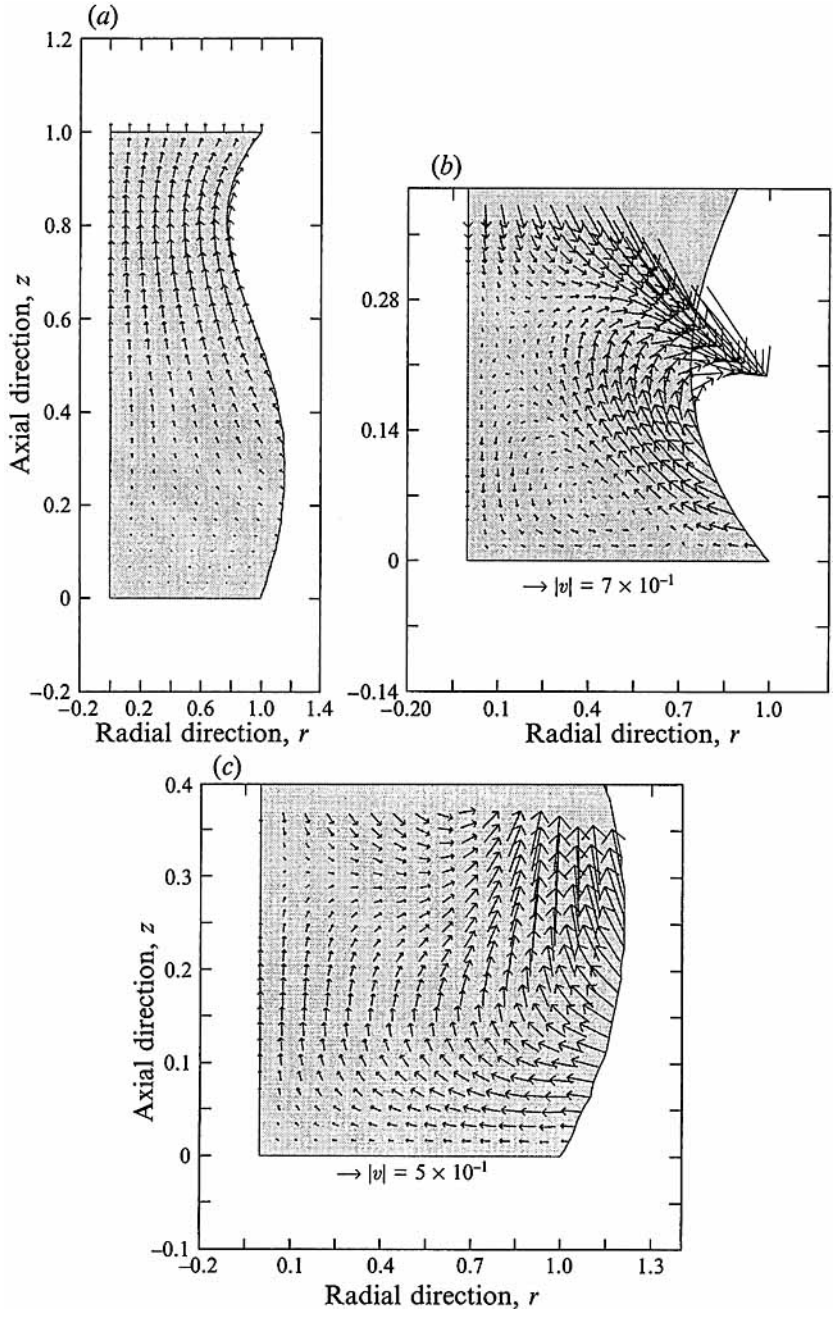

FIGURE 9. (*a*) Velocity field of first mode calculated using inviscid analysis, $\Lambda = 1.2/\pi$ and $\sigma = 1.921$, and magnification of the flow field at the bottom of a bridge with $Re = 30$, $\Lambda = 1/\pi$, $\alpha = 0.2$ and $\sigma = 1.117$ at (*b*) $t = 3.142$ and (*c*) $t = 5.619$.

Subsequently, the top plate reverses its motion and an unsteady internal layer is created owing to the collision of fluid close to the upper wall which starts moving downwards with fluid from the mid-plane which still moves upwards owing to its inertia. As time progresses this internal layer is located lower in the bridge. At $t = \pi$,

the same internal layer interacts with fluid close to the lower solid surface and creates recirculation throughout the lower third of the bridge which eventually dissipates. Unfortunately, this cannot be clearly seen in figure 8, because the velocity field is much weaker there. However, it can be seen in figure 9 where it has been preferentially magnified. When the downward velocity of the upper rod passes its maximum value, $t > \pi$, fluid near the upper (lower) solid surface starts moving towards (away from) the centreline. At about $t = \frac{4}{3}\pi$ as well as at $t = \frac{1}{3}\pi$, the interface shape of the bridge becomes almost cylindrical. At $t = \frac{3}{2}\pi \approx 4.712$ the upper plate starts moving upwards. This creates internal layers near the both solid/liquid interfaces, shown here at $t = 5.079$. In contrast to the earlier one, the upper internal layer is now created because nearby fluid elements tend to move in opposite directions. Complicated recirculation patterns may be seen throughout the lower third of the bridge at $t = 5.619$. Finally at $t = 2\pi = 6.283$ the flow field has completed its cycle and has reached its original configuration.

At even lower values of Re, fluid recirculation damps out faster and is limited to the upper part of the bridge. Clearly, with very viscous fluids the motion would become rotational and creeping throughout. Given the results of linear analysis this should be expected at $Re < 2$. On the other hand, at higher values of Re viscous dissipation should be confined in the boundary layers near the two solid surfaces, as described in Borkar & Tsamopoulos (1991).

The flow field presented above can be easily contrasted to that obtained from inviscid analysis or the one-dimensional Cosserat model. Figure 9 shows a magnification of the viscous flow field in the lower part of the bridge at two instances along with the inviscid flow field at any point in time. The latter is calculated by the zeroth-order (in $1/Re$) solution given in Borkar & Tsamopoulos (1991) which is similar to the inviscid result in Sanz (1985). In order to obtain the inviscid solution at any other time instant, t, the numerical values in figure 9 must be multiplied by $\cos(t)$. The flow is now mostly confined to the free surface and the middle part of the bridge. Obviously, no recirculation, internal layers, or boundary layers can be predicted by the inviscid analysis. Moreover, there is inward (outward) velocity along the upper (lower) solid/liquid surface, since the no-slip condition is not satisfied. Only this effect is remedied by the boundary-layer analysis (Borkar & Tsamopoulos 1991), which, nevertheless, cannot predict either internal layers or regions of recirculation. This is the reason why there is significant deviation for $Re \leqslant 50$ between predictions of the boundary layer and viscous theories. This deviation is even more apparent in the damping rates and for higher modes.

4.2. *Nonlinear damping rate*

In a similar manner it should be expected that nonlinearities will modify the damping rate from its linear values. Upon obtaining resonance conditions for a given set of Re, Λ, and α, motion of the upper rod is stopped by setting its velocity to zero as soon as the rod reaches the location $z = 1$. In spite of this, the liquid bridge is driven by inertia and continues its motion which for the range of Re examined is underdamped, owing to viscous dissipation in the liquid. Simulations are stopped when the overall amplitude of deformation is close to zero. Figure 10 shows the variation of A_d/α *vs.* time in a typical free oscillation. Given the definition of A_d two maxima and two minima comprise a complete period.

In the linear analysis by Tsamopoulos *et al.* (1992), time was scaled by $(\rho R^3/\gamma)^{\frac{1}{2}}$ since there was no other characteristic time in that system. Here however, it was more convenient to use the inverse of the forcing frequency as a characteristic time.

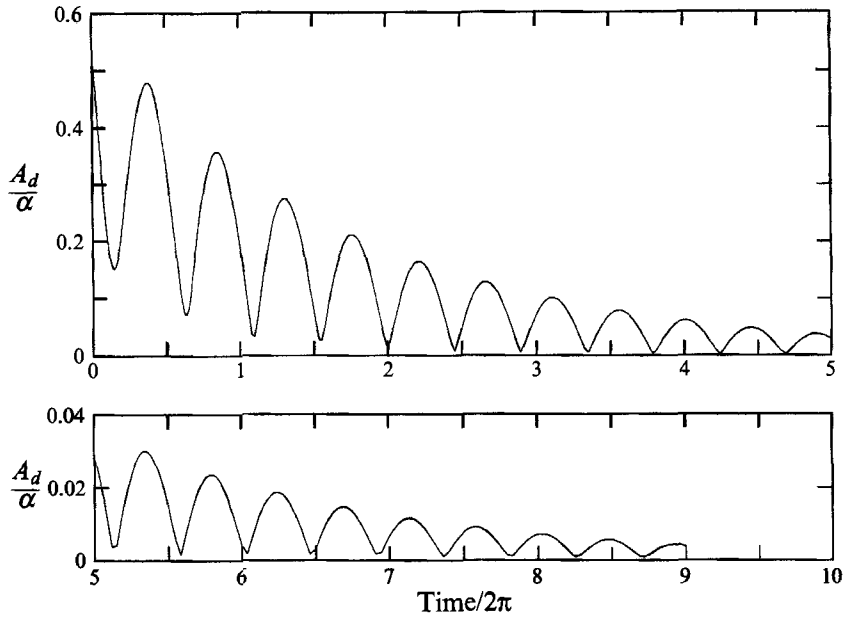

FIGURE 10. Evolution of the interface amplitude of a liquid bridge in free oscillation after resonance was achieved with $Re = 20$, $\Lambda = 1/\pi$, $\sigma = 1.15$ and $\alpha = 0.2$.

Therefore, the damping rate calculated by the linear analysis must be adjusted as follows:

$$\sigma_D^L = \sigma_R^L / \sigma_I^L \,, \tag{4.1}$$

in order to relate it to the present results. In (4.1) σ_R^L and σ_I^L are the linear damping rate and linear eigenfrequency with respect to the scaling in the linear theory, respectively, and σ_D^L is the linear damping rate according to the present definition of characteristic time.

Each mark in figure 11 and figures thereafter represents $A_{d,max}/\alpha$ at different points in time, where $A_{d,max}$ is the maximum value of A_d in each half-cycle. The marks have been connected by a smooth curve. As noted earlier there are two maxima in each cycle. In damped oscillations the maxima correspond to inward (outward) motion of the upper (lower) part of the bridge and vice versa. If the linear damping is considered, then

$$\left(\frac{A_{d,max}}{\alpha}\right)_t = \left(\frac{A_{d,max}}{\alpha}\right)_{t_1} \exp\left[-(t-t_1)\,\sigma_D^L\right] \tag{4.2}$$

relates the reduced overall amplitude of the first maximum at time t_1 to its value at subsequent points in time. Starting from the same first maximum the curve produced by (4.2) lies above the nonlinear data and therefore it predicts smaller damping than the nonlinear analysis. The nonlinear data exhibit a larger slope at the beginning of free oscillations and a smaller slope later on. Therefore, they do not follow a single exponential curve and the damping rate has become amplitude or time dependent.

Experimentally, it is easier to identify the first few maxima in amplitude since they are larger. Therefore, the first two maxima from the nonlinear analysis will be used in (4.2) and the resulting value of σ_D^{NL} will be called the nonlinear damping rate. A similar procedure is used in measuring experimentally σ_D^{NL}, see Mollot *et al.* (1993).

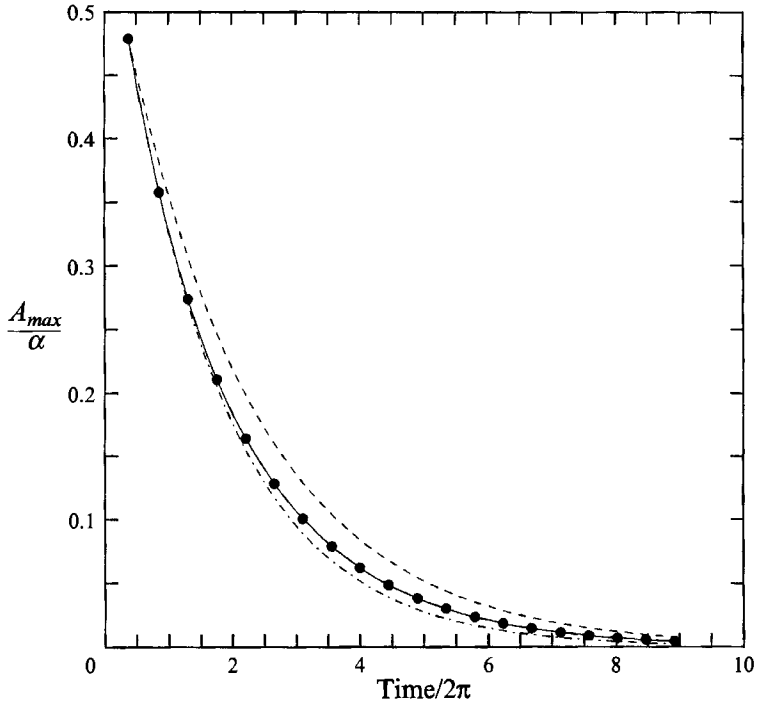

FIGURE 11. Comparison of nonlinear damping (—●—), linear damping (– – –) using $\sigma_D^L = 0.07657$ and damping by fitting an exponential through the first two nonlinear points (–·–·–) using $\sigma_D^{NL} = 0.09828$, for $Re = 20$, $\Lambda = 1/\pi$, $\alpha = 0.2$ and $\sigma = 1.15$.

α	Re	$\Lambda\pi$	Linear damping rate	Linearized nonlinear damping rate	Percentage change
Infinitesimal	20	1	0.0766	—	—
0.1	20	1	—	0.0860	12.3
0.2	20	1	—	0.0983	28.3
0.3	20	1	—	0.1066	39.2
Infinitesimal	20	0.75	0.0830	—	—
0.2	20	0.75	—	0.0976	17.6
Infinitesimal	20	1.25	0.0786	—	—
0.2	20	1.25	—	0.121	53.9
Infinitesimal	10	1	0.147	—	—
0.2	10	1	—	0.161	9.5
Infinitesimal	30	1	0.0526	—	—
0.2	30	1	—	0.0682	29.7
Infinitesimal	50	1	0.0329	—	—
0.2	50	1	—	0.0522	58.7

TABLE 3. Effect of forcing amplitude, α; fluid properties, Re; and bridge geometry, Λ on damping rate of liquid bridge

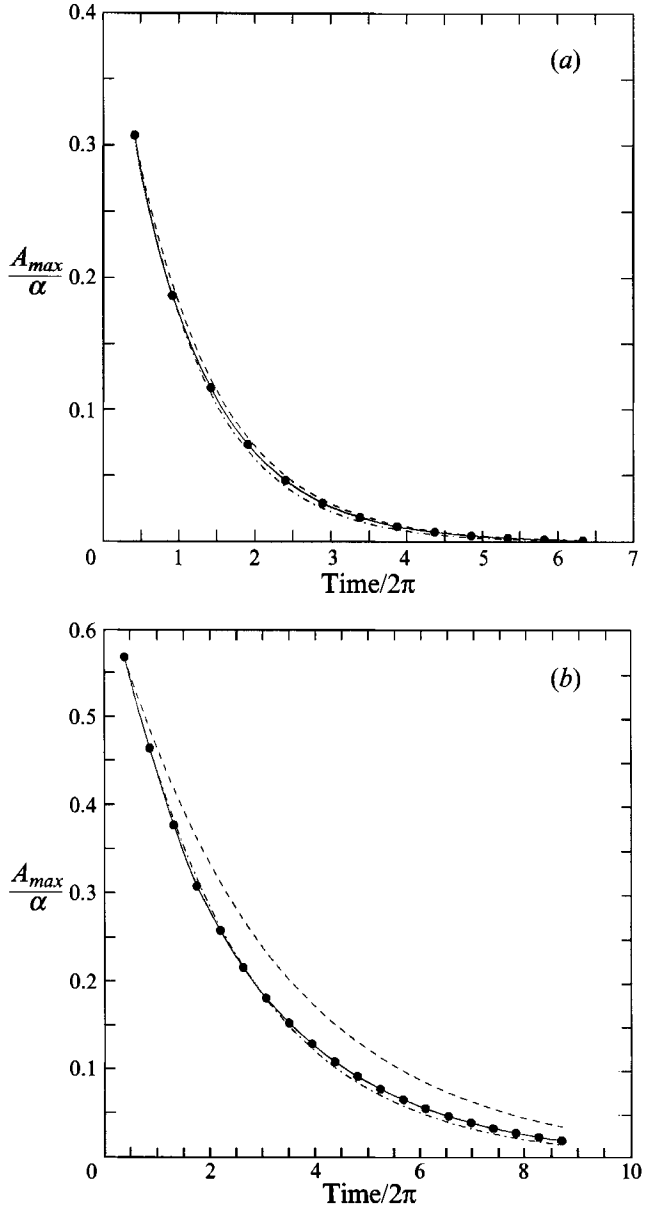

FIGURE 12. Comparison of nonlinear damping (—●—), linear damping (——) with (*a*) $\sigma_D^L = 0.147$, (*b*) $\sigma_D^L = 0.05264$, and damping by fitting an exponential through the first two nonlinear points (–·–·–) with (*a*) $\sigma_D^{NL} = 0.161$, (*b*) $\sigma_D^{NL} = 0.0682$, for (*a*) $Re = 10$, $\Lambda = 1/\pi$, $\alpha = 0.2$, $\sigma = 1.25$ and (*b*) $Re = 30$, $\Lambda = 1/\pi$, $\alpha = 0.2$, $\sigma = 1.117$.

Using this value of σ_D^{NL} a new exponential curve may be generated which lies slightly below the nonlinear data at later times. Figure 11 shows that the nonlinear data are bracketed from above by the exponential curve created by the linear theory and from below by the exponential curve created from the first two maxima. At the beginning of free oscillations, deformation and velocity are large enough, so that viscous dissipation is larger. Later on, they become very small and the nonlinear data approach asymptotically the prediction of linear theory. Similar behaviour was found with $\alpha =$

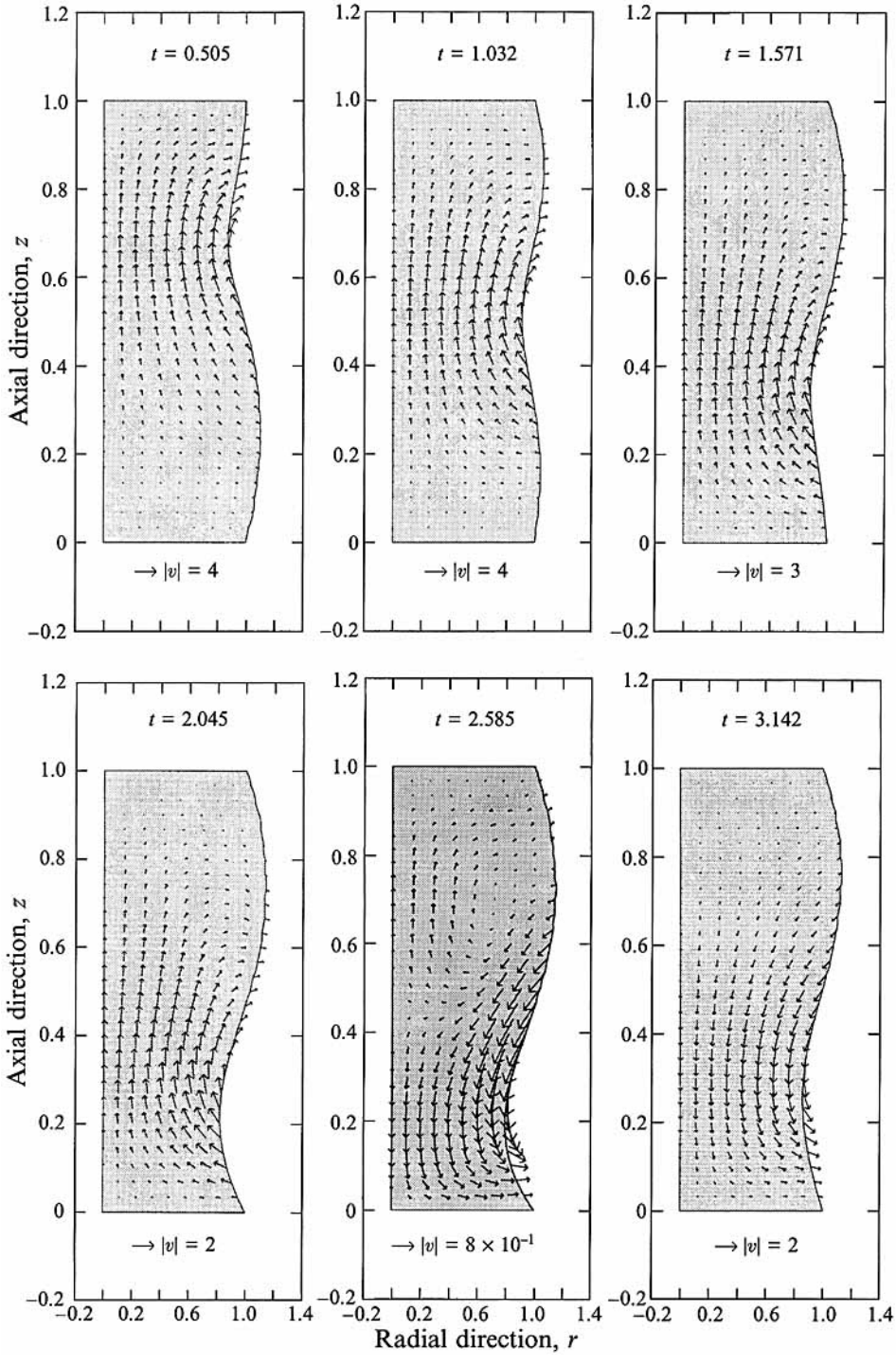

FIGURE 13. For caption see facing page.

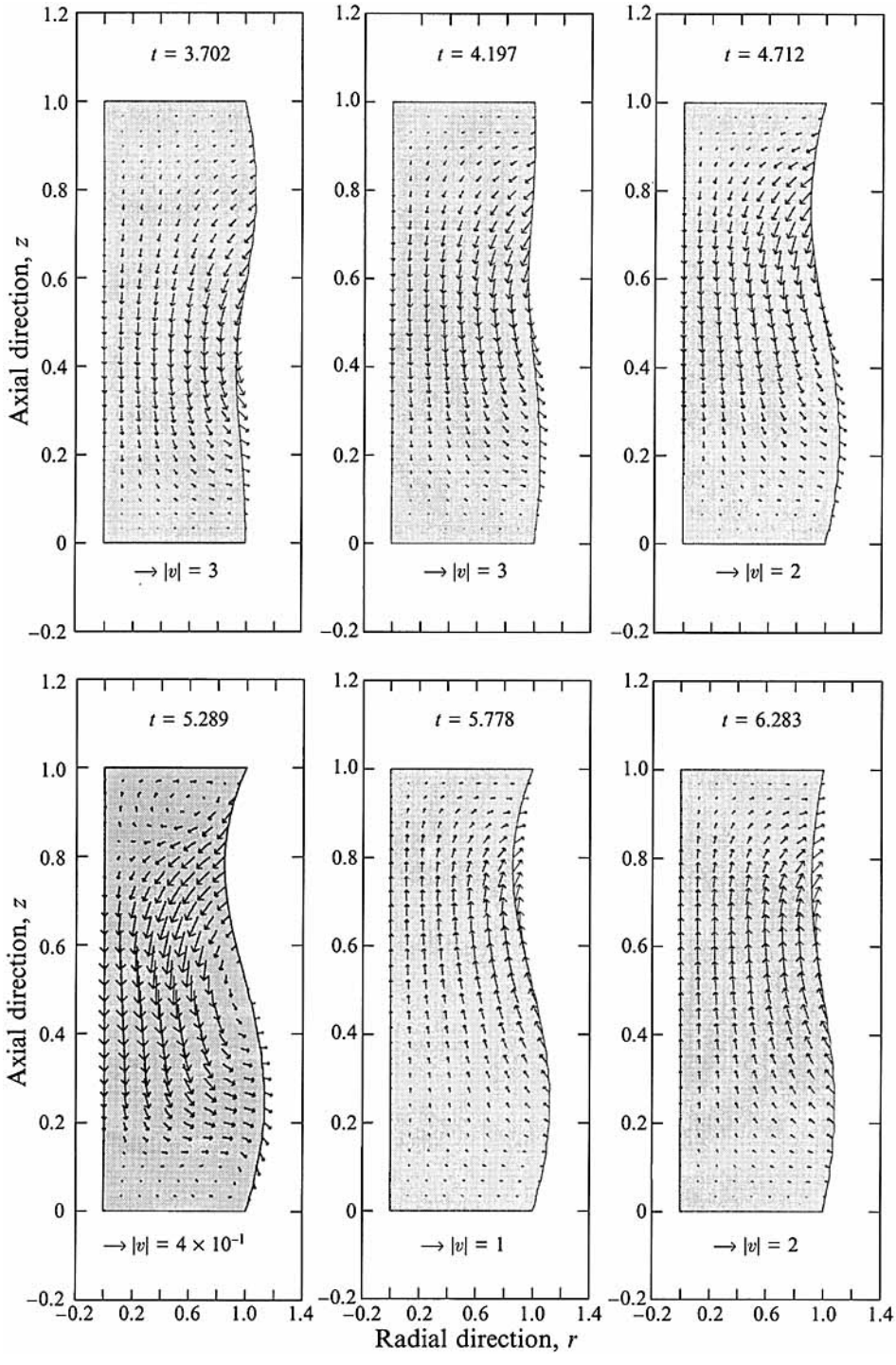

FIGURE 13. Velocity field of a liquid bridge in free oscillation after resonance was achieved with $Re = 30$, $\Lambda = 1/\pi$, $\alpha = 0.2$, and $\sigma = 1.117$.

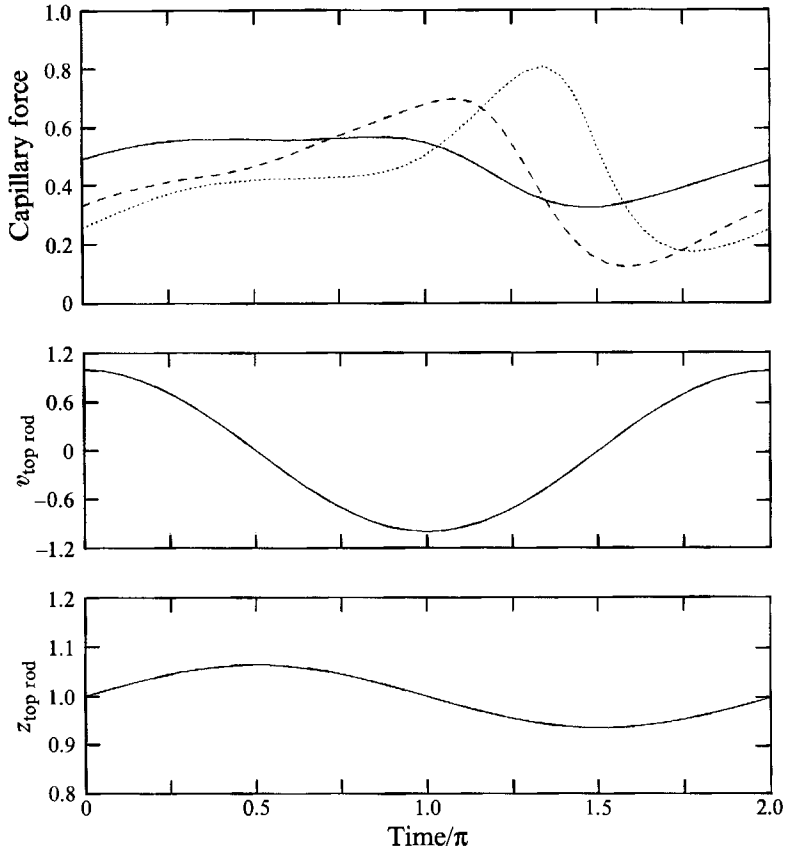

FIGURE 14. Evolution of capillary force, velocity of top rod, and position of top rod in one period of forced oscillation. For the capillary force, ——, – – –, and ·····, indicate $\sigma = 1.025$, 1.150 (resonance frequency), and 1.325, respectively.

0.1, and $\alpha = 0.3$. Comparing the calculated values shown in table 3 indicates that the nonlinear damping rate increases with the amplitude of the initial disturbance. This should be expected, since motion with a larger amplitude should induce stronger recirculation and even internal layers which dissipate it faster. From the same table it may be observed that as a bridge of given radius becomes shorter (larger A) the nonlinear damping rate deviates further from the linear one. Since in all cases free oscillations start from resonance conditions, larger values of A correspond to larger values of nonlinear frequency (see figure 6), which are a measure of the velocity field ($\overline{A\omega}$). This stronger velocity field in a more confined region would dissipate faster. Additional plots of the amplitude evolution in free oscillations are given in Chen (1991).

Figures 11 and 12 along with table 3 show the effect of Re on the damping rate. At $Re = 10$ the motion is nearly dominated by viscous effects and inertia plays a small role. Fewer and shorter maxima in A_d/α are found. This would require increased attention in experimentally measuring damping rates. Moreover, the nonlinear damping rate follows quite closely the linear one. On the other hand, at $Re \geqslant 30$ motion dissipates much slower so that enough oscillation periods are observed. Therefore, it is now easier to measure damping rates although they deviate significantly from their linear values. Thus, the dynamics of liquid bridges in free oscillation are

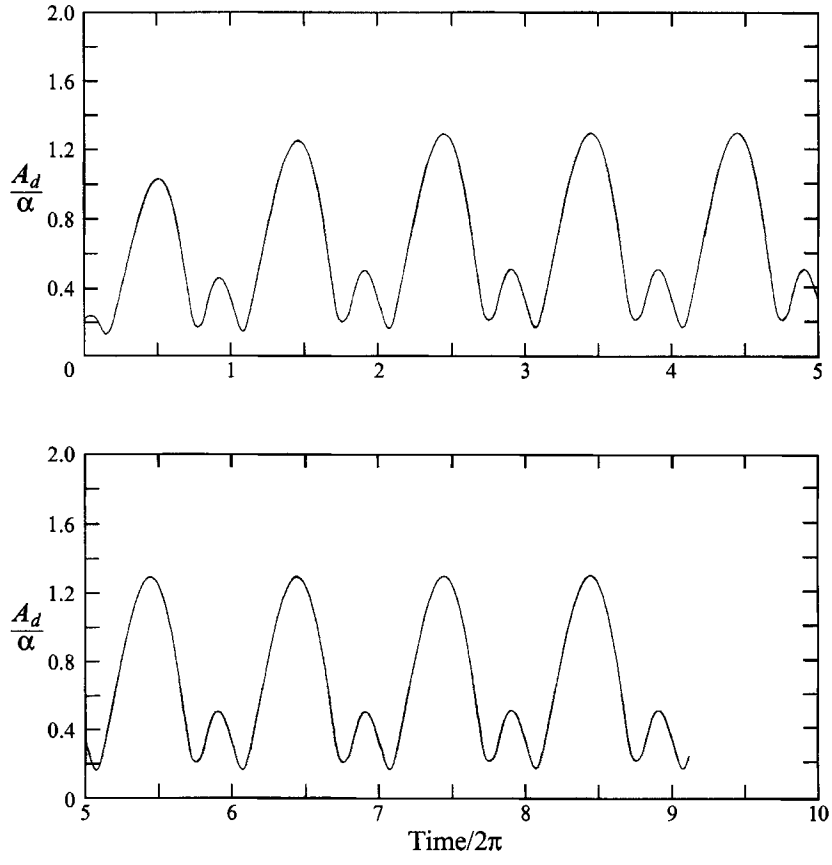

FIGURE 15. Amplitude evolution of a liquid bridge with $B = 0.2\pi$, Re = 20, $\Lambda = 1/\pi$, $\alpha = 0.2$, and $\sigma = 0.925$.

parallel to either surface levelling of a very viscous liquid (overdamped) or to capillary waves of an inviscid liquid (underdamped).

Figure 13 shows the velocity field during free oscillations at intervals of approximately $\frac{1}{6}\pi$. The conditions are the same as those in figure 8. Substantial motion of the liquid may be observed and is caused by its inertia. Eventually, the kinetic energy is attenuated by viscosity and in the absence of gravity the bridge returns to its original shape, the cylindrical one. Internal layers and recirculation may be seen at the centre of the bridge or close to the solid/liquid interfaces at $t = 2.585$ and 5.289, respectively. Both will expedite energy attenuation. For easier observation these cases are shown at twice the resolution of the rest.

4.3. *Force on the lower solid surface*

As an alternative means of monitoring the bridge motion, one may measure the total force acting on the lower rod. Its variation with time in comparison with the location of the upper rod may provide useful information on the liquid in the bridge. The feasibility of this approach and a comparison of experimental measurements to a first-order theory is given in Ennis *et al.* (1990). Their simplified theory combines the lubrication approximation with static capillary forces. Their primary interest is in estimating the force caused by a very short liquid bridge which connects two spherical particles. In general, the total force acting on the lower rod varies during a period of

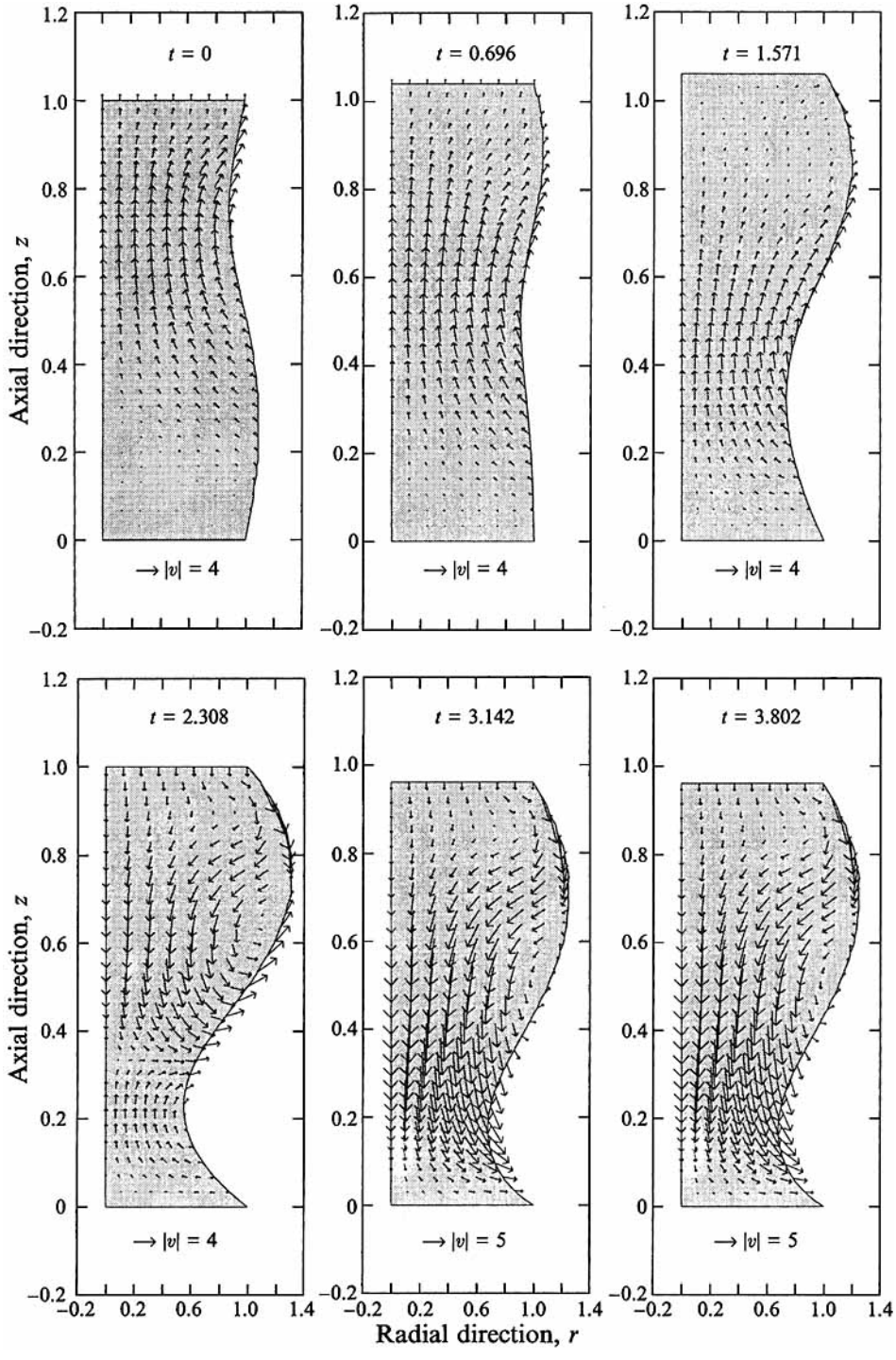

FIGURE 16. For caption see facing page.

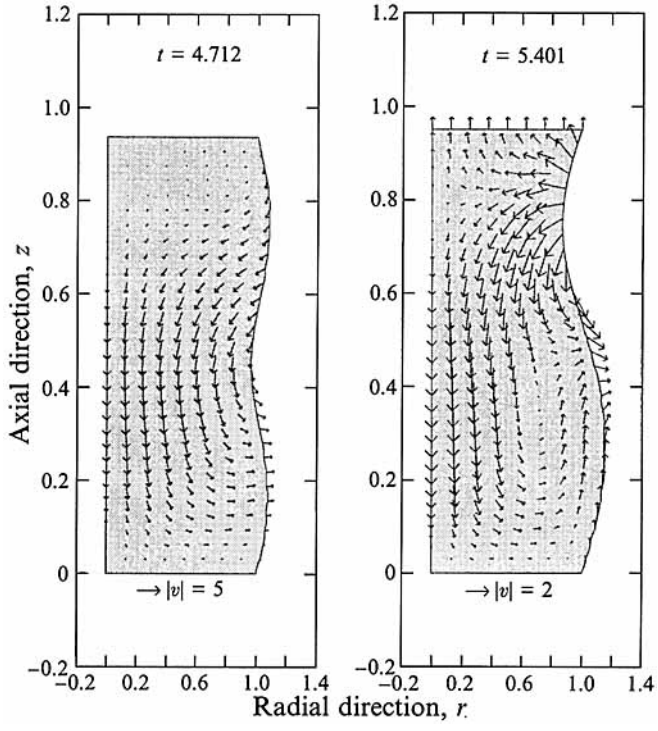

FIGURE 16. Velocity field and interface shape of a liquid bridge oscillating at resonance in the gravitational field, with $Re = 20$, $\Lambda = 1/\pi$, $\alpha = 0.2$, $\sigma = 0.925$, and $B = 0.2\pi$.

oscillation and it is composed of a surface tension contribution, $2\pi\bar{R}\gamma\sin(\theta_c)$, and a pressure contribution,

$$2\pi\int_0^{\bar{R}}(\bar{P}_i-\bar{P}_o)|_{z=0}\,\bar{r}\,\mathrm{d}\bar{r}.$$

The former opposes separation of the rods since $0 \leqslant \theta_c \leqslant 180°$ always; whereas the latter opposes their separation if $\bar{P}_i < \bar{P}_o$. Here P_i and P_o are the pressures inside and outside the gas/liquid interface, respectively, and θ_c is the contact angle at the edge of the lower rod measured through the liquid phase. θ_c is defined as

$$\theta_c = \cos^{-1}(\boldsymbol{e}_z\cdot\boldsymbol{N}), \tag{4.3}$$

where the unit outward normal vector on the free surface, $\boldsymbol{N}$, is evaluated at $z = 0$. Since the supporting surface is flat, the viscous normal stress can be shown to be identically zero by combining (2.1) and (2.5*a*). Thus, the total force on the bottom rod is given by

$$\bar{F} = 2\pi\bar{R}\gamma\sin(\theta_c) - 2\pi\int_0^{\bar{R}}(\bar{P}_i-\bar{P}_o)|_{\bar{z}=0}\,\bar{r}\,\mathrm{d}\bar{r}. \tag{4.4}$$

The force may be scaled by $2\pi\bar{R}\gamma$ and thus (4.4) becomes

$$F = \sin(\theta_c) - \int_0^1 (P_i-P_o)|_{z=0}\,r\,\mathrm{d}r. \tag{4.5}$$

According to (4.5) the lower rod experiences an upward (downward) force, if F is positive (negative).

Figure 14 shows the total force acting on the lower rod, along with the oscillating velocity and position of the upper rod in a typical forced-oscillation cycle. The total

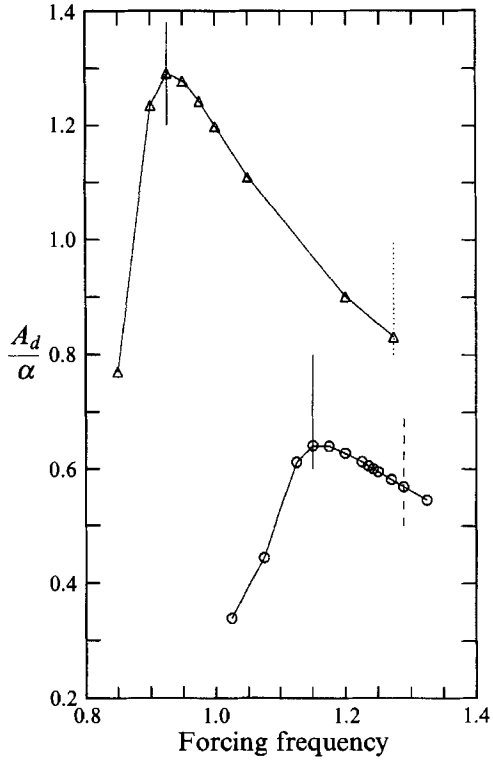

FIGURE 17. Shift of frequency at resonance of a liquid bridge with $B = 0.2\pi$ (△, nonlinear or ···, linear analysis) and $B = 0$ (○, nonlinear or ——, linear analysis), for $Re = 20$, $\Lambda = 1/\pi$, and $\alpha = 0.2$. The vertical solid lines indicate nonlinear resonance frequencies. The dashed lines represent linear eigenfrequencies of each case.

capillary force in a static and cylindrical liquid bridge may be readily calculated, since then, $\theta_c = 90°$ and $P_i - P_o = 1$ and therefore $F = 0.5$. The departure of F from this value is brought about by the fluid motion which alters both θ_c and P_i during oscillation; see figure 8. The maximum value of F in a period occurs after the point of maximum separation between the rods and when the interface shape is concave in the region $z = 0$. Then, both the surface curvature and viscous contribution to $P_i - P_o$ are very small; see figure 8 at $t = 2.588$, 3.142 and 3.610. In addition, this maximum value of F arises at later times when the forcing frequency increases. This is a direct result of the increased inertia of the system, see (2.2), and has been found experimentally by Ennis *et al.* (1990), as well.

4.4. *Gravitational effects*

In a typical experimental study on Earth the gravitational Bond number, B, is different from zero. For example, in the experiments carried out by Mollot *et al.* (1993) B usually varied between 0.3 and 0.6. Therefore, the effect of gravity on the nonlinear bridge dynamics must be examined.

Figure 15 shows that a viscous liquid bridge achieves a steady oscillatory motion fairly fast. In this and all other calculations with $B \neq 0$ the initial shape is that of static bridge at the same Bond number and with liquid volume the same as the volume of the space between the cylindrical rods. Although two maxima in amplitude still exist in every oscillation cycle, they are seen in figure 15 to be very different in magnitude. The larger one occurs when the top rod starts pushing downwards from its point of

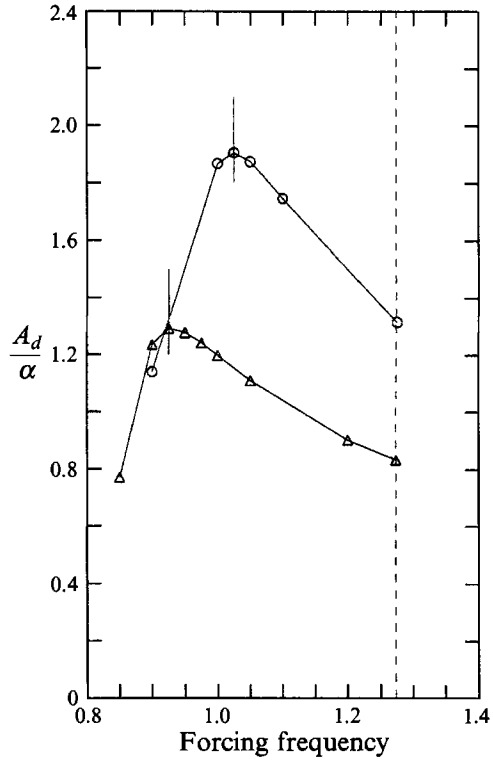

FIGURE 18. Shift of resonance frequency of a liquid bridge with $B = 0.2\pi$, $Re = 20$ and $\Lambda = 1/\pi$. Dashed line (----) indicates the linear eigenfrequency and solid lines represent resonant frequencies for $\alpha = 0.1$ (○) and $\alpha = 0.2$ (△).

		Linear		Nonlinear		Percentage change	
α	B	frequency	damping	frequency	damping	frequency	damping
Infinitesimal	0.628	1.273	0.0745	—	—	—	—
0.1	0.628	—	—	1.025	0.0842	−19.5	13.0
0.2	0.628	—	—	0.925	0.1031[1]	−27.3	38.4
—	—	—	—	—	0.0942[2]	—	26.4

[1] Forced oscillations are stopped at $z = 1$ while the top rod is moving upwards.
[2] Forced oscillations are stopped at $z = 1$ while the top rod is moving downwards.

TABLE 4. Effect of forcing amplitude α and Bond number, B, on resonant frequency and damping rate of a liquid bridge at $Re = 20$ and $\Lambda = 1/\pi$

maximum separation from the lower rod; whereas the smaller one occurs when the top rod starts pulling upwards from the point of minimum separation. In comparison with the case of $B = 0$ (figure 2), this more (less) deformed interface in the two different stages of motion results from the fact that the acceleration induced by the rod oscillation and gravity are additive (subtractive). Interface shapes and velocity fields for $B = \frac{1}{5}\pi = 0.628$, $Re = 20$, $\Lambda = 1/\pi$ and $\alpha = 0.2$ at resonance are shown in figure 16. Areas of recirculation and internal layers may be readily seen, for example at $t = 2.308$, 3.142, 3.802, 5.401. Although the bridge geometry and oscillation amplitude are the same as in figure 8 and Re somewhat smaller, recirculation seems to appear more often

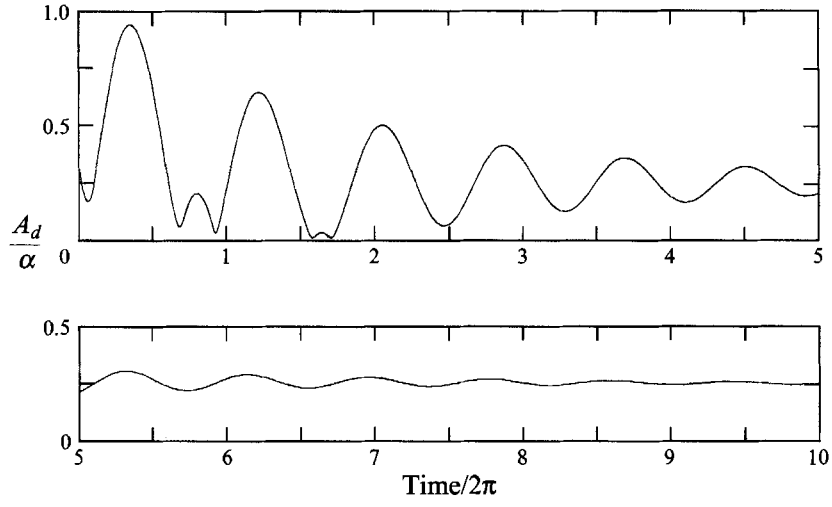

FIGURE 19. Evolution of amplitude of a liquid bridge in free oscillation when the top rod stops at the end of the complete period of oscillation, with $Re = 20$, $B = 0.2\pi$, $\Lambda = 1/\pi$, $\alpha = 0.2$, and $\sigma = 0.925$.

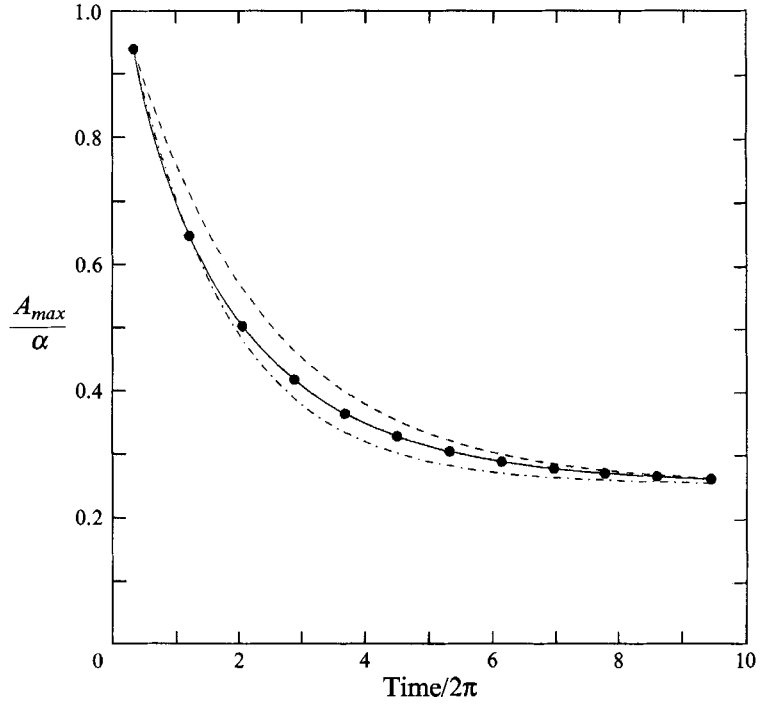

FIGURE 20. Comparison of nonlinear damping (—●—), linear damping (– – –) using $\sigma_D^L = 0.0745$; and damping by fitting an exponential through the first two nonlinear points (– · – · –) using $\sigma_D^{NL} = 0.1031$, with $Re = 20$, $B = 0.2\pi$, $\Lambda = 1/\pi$, $\alpha = 0.2$, and $\sigma = 0.925$.

and it is stronger. This is because gravity increased bridge deformations which in turn facilitate fluid recirculation.

According to linear theory, the eigenfrequency of a capillary bridge decreases as the Bond number increases. This is because the unperturbed static shape with $B \neq 0$ resembles more the first oscillation mode than the static shape with $B = 0$ (cylindrical),

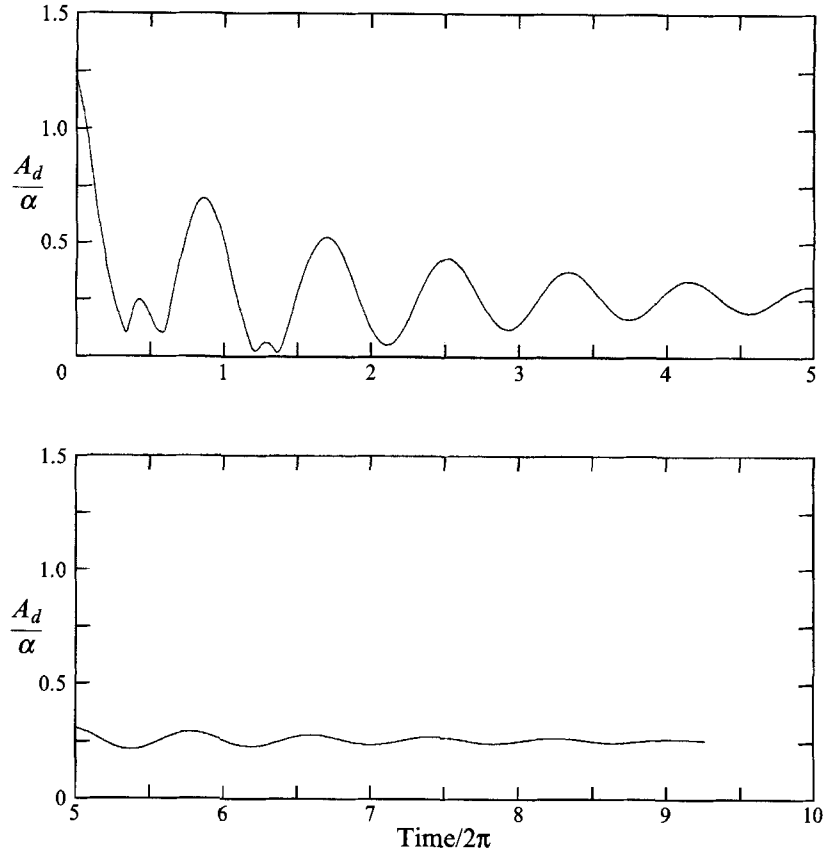

FIGURE 21. Amplitude evolution of a liquid bridge in free oscillation when the top rods stops after half a period of oscillation with $Re = 20$, $B = 0.2\pi$, $A = 1/\pi$, $\alpha = 0.2$, and $\sigma = 0.925$.

Thus, the former is easier to excite. When gravity and nonlinearity are considered simultaneously, resonant frequencies decrease even more. Figure 17 shows that the small difference in linear frequencies between a case with $B = 0$ and one with $B \neq 0$ is considerably increased when nonlinear effects are accounted for, see also table 4. In analogy with the $B = 0$ case, larger amplitudes cause larger decreases in resonant frequencies, see figure 18.

Damping rates are calculated as in the case with $B = 0$. The upper rod is stopped at $z = 1$ and after resonance conditions were reached. The variation of A_d/α is recorded till the bridge returns to its static configuration. The static value of A_d/α for $B \neq 0$ is larger than zero. This static value will be indicated by $(A_d/\alpha)_{t_\infty}$. Therefore, the amplitude predicted from linear theory should vary according to the following equation:

$$\left(\frac{A_{d,max}}{\alpha}\right)_t = \left[\left(\frac{A_{d,max}}{\alpha}\right)_{t_1} - \left(\frac{A_d}{\alpha}\right)_{t_\infty}\right] \exp\left[-(t-t_1)\,\sigma_D^L\right] + \left(\frac{A_d}{\alpha}\right)_{t_\infty}. \tag{4.6}$$

The rest of the terms were defined earlier. Damped oscillations for $\alpha = 0.2$ are shown in figure 19. The upper rod is stopped at $z = 1$ during its upward motion, i.e. when it has just completed a full cycle, $t = 2\pi$. The final value of A_d/α is 0.25, which is its static value. The larger maxima in each cycle from figure 19 are shown in figure 20, which also shows the amplitude variation according to linear theory and by fitting an

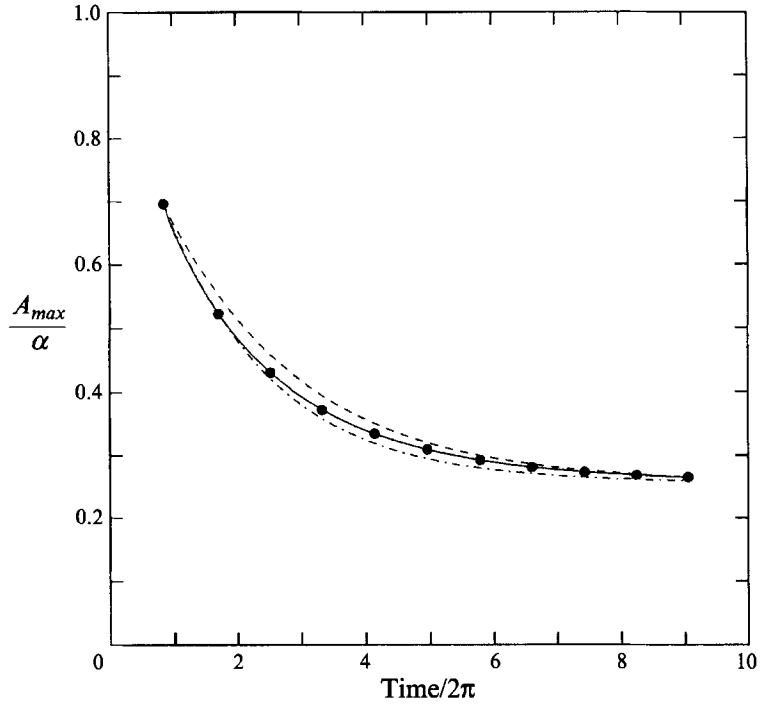

FIGURE 22. Comparison of nonlinear damping (—●—), linear damping (– – –) using $\sigma_D^L = 0.0745$ and damping by fitting an exponential through the first two nonlinear points (–·–·–) using $\sigma_D^{NL} = 0.0942$ with $Re = 20$, $B = 0.2\pi$, $\Lambda = 1/\pi$, $\alpha = 0.2$, and $\sigma = 0.925$.

exponential curve through the first two points. Similar calculations, but with $\alpha = 0.1$ are reported in Chen (1991). Again, larger-amplitude motions damp out faster and as time increases they approach the linear result.

Since with $B \neq 0$ there are two maxima with very different magnitudes in each cycle (see figure 15) damping rates may be affected by the time at which forced oscillations are stopped. Indeed, when the top rod is stopped at $z = 1$, but during its downward motion ($t = \pi$) a slightly different result is obtained. Figures 21 and 22 show the resulting amplitude variation with time and its maximum values for conditions identical to figures 19 and 20, respectively. It may be seen that σ_D^{NL} has decreased somewhat. This may be explained by observing that now the first maximum in the free oscillations arises later in time and is smaller. As a result, the flow has already slightly dissipated and the damping rate deviates less from the predictions of linear theory.

5. Concluding remarks

The nonlinear dynamics of capillary bridges have been examined. It was found that finite-amplitude forced oscillations have lower resonant frequencies than those predicted by linear theory. The decrease in frequency depends almost linearly on the amplitude for the range of *Re* examined. Also, finite-amplitude free oscillations exhibit larger damping rates which are time dependent and as the amplitude gets smaller they approach the corresponding linear values. Furthermore, the frequency decrease and damping rate increase become more prominent for larger *Re* or shorter bridges. Gravity may affect significantly the resonant frequency and damping rate, depending

Material	Temperature (°C)	Surface tension (dynes/cm)	Density (g/cm^3)	Viscosity (cP)	Modified *Re*	Reference
Bi-garnet doped by WO_3	850	177	7.8	25	47	Luther (1986)
$LiCaAlF_6$	820	167.3	2.501	18.4	35	Fratello & Brandle (1991)
$Y_3Al_5O_{12}$	2000	781	3.684	43.5	39	Fratello & Brandle (1993)
B_2O_3	1100	88	1.514	5800	0.06	Mackenzie (1956); Kingery (1959)

TABLE 5. Properties of materials with modified $Re < 100$

on the size of the liquid bridge and the density of the liquid, i.e. the gravitational Bond number.

It is well-known that static shapes of capillary bridges or pendant drops can provide a very accurate estimation of surface tension (Padday 1971). As noted in Tsamopoulos *et al.* (1992) and further elaborated here the resonance frequency and damping rate of an oscillating bridge can provide an accurate measurement of surface tension and viscosity of the liquid in the bridge, if the modified $Re < 100$. Several molten materials of current interest such as refractories, laser hosts, etc., fulfil this requirement. A small sample is given in table 5. Generally, alkali borates and silicates of different compositions and at different temperatures cover the whole range of $0 \leqslant Re \leqslant 100$.

Since the damping rate is time-dependent, it seems more appropriate to measure surface tension by a static method and viscosity by measuring the resonance frequency of the bridge. According to the static method one needs to compare the observed static bridge shapes to calculated ones for various B. Subsequently, the resonance frequency of the bridge or its damping rate can be measured experimentally as described in Mollot *et al.* (1993). These values can be compared to the linear results given in Tsamopoulos *et al.* (1992) (e.g. their figure 4) for a preliminary calculation of Re and estimation of the viscosity. Then tables such as table 2 or 3 given here can be employed so that nonlinear effects will be accounted for. The accuracy to which viscosity can be deduced depends on the accuracy to which the resonance frequency can be measured. For example, using data from table 2 with $Re \sim 20$, $\alpha = 0.2$ and $\Lambda = 1/\pi$ we find that measuring the resonance frequency with an accuracy of 2–3 Hz, will result in viscosity predictions with an accuracy of 1 cP. For further details see Mollot *et al.* (1993). As noted earlier, the present method is even more sensitive if higher modes are excited, if larger-amplitude motions are achieved, or if the damping rates can be measured as accurately as the resonance frequencies.

This work has been partially supported by the DOE, Grant No DE-AC22-87DC-79905 and by the Fluid Mechanics Program of NSF under Grant No. MSM-8705735. Use of the Cornell National Supercomputer Facilities (CNSF) and the graphics software developed by Dr A. Poslinski are gratefully acknowledged.

REFERENCES

BASARAN, O. A. 1992 Nonlinear oscillations of viscous liquid drop. *J. Fluid Mech.* **241**, 169–198.

BENJAMIN, T. B. & SCOTT, J. C. 1979 Gravity–capillary waves with edge constraints. *J. Fluid Mech.* **92**, 241–267.

BORKAR, A. & TSAMOPOULOS, J. A. 1991 Boundary-layer analysis of the dynamics of axisymmetric capillary bridges. *Phys. Fluids* A **3**, 2866–2874.

BROWN, R. A. 1988 Theory of transport processes in single crystal growth from the melt. *AIChE J.* **34**, 881–911.

CHEN, T.-Y. 1991 Static and dynamic analysis of capillary bridges. PhD thesis, State University of New York at Buffalo.

CHEN, T.-Y., TSAMOPOULOS, J. A. & GOOD, R. J. 1991 Capillary bridges between parallel and non-parallel surfaces and their stability. *J. Colloid Interface Sci.* **151**, 49–69.

DERBY, J. J. & BROWN, R. A. 1986 A fully implicit method for simulation of the one-dimensional solidification of a binary alloy. *Chem. Engng Sci.* **41**, 37–46.

DURANCEAU, J. L. & BROWN, R. A. 1986 Thermal capillary analysis of small-scale floating zones: Steady-state calculations. *J. Cryst. Growth* **75**, 367–389.

DURANCEAU, J. L. & BROWN, R. A. 1988 Finite element analysis of melt convection and interface morphology in earthbound and microgravity floating zones. *AIP Conf. Proc.* vol. 197 (ed. T. G. Wang), pp. 133–144.

ENNIS, B., LI, J., TARDOS, G. & PFEFFER, R. 1990 The influence of viscosity on the strength of an axially strained pendular liquid bridge. *Chem. Engng Sci.* **45**, 3071–3088.

ETTOUNEY, H. M. & BROWN, R. A. 1983 Finite element methods for steady solidification problems. *J. Comput. Phys.* **49**, 118–150.

FOWLE, A. A., WANG, C. A. & STRONG, P. F. 1979 Experiments on the stability of conical and cylindrical liquid columns at low Bond numbers. *Arthur D. Little Co.* Ref. C-82435.

FRATELLO, V. J. & BRANDTLE, C. D. 1991 Thermophysical properties of $LiCaAlF_6$ melt. *J. Cryst. Growth* **109**, 334–339.

FRATELLO, V. J. & BRANDTL, C. D. 1993 Physical properties of $Y_3Al_5O_{12}$ melt. *J. Cryst. Growth* (to appear).

GRESHO, P. M., LEE, R. L. & SANI, R. L. 1980 On the time-dependent solution of the incompressible Navier–Stokes equations in two and three dimensions. In *Recent Adv. Numer. Meth. Fluids*, vol. 1 (ed. C. Taylor & K. Morgan), pp. 27–79. Swansea: Pineridge.

HARRIOTT, G. M. & BROWN, R. A. 1984 Flow in a differentially rotated cylindrical drop at moderate Reynolds number. *J. Fluid Mech.* **144**, 403–418.

KEUNINGS, R. 1986 An algorithm for the simulation of transient viscoelastic flows with free surfaces. *J. Comput. Phys.* **62**, 199–220.

KHESHGI, H. S. & SCRIVEN, L. E. 1984 Penalty finite element analysis of unsteady free-surface flows. In *Finite Elements in Fluids*, vol. 5 (ed. R. H. Gallagher, J. T. Oden, O. C. Zienkiewicz, T. Kawai & M. Kawahara), pp. 393–434. John Wiley & Sons.

KINGERY, W. D. 1959 Surface tension of some liquid oxides and their temperature coefficients, *J. Am. Ceram. Soc.* **42**, 6–10.

KISTLER, S. F. & SCRIVEN, L. E. 1983 Coating flows. In *Computational Analysis of Polymer Processing* (ed. J. R. A. Pearson & S. M. Richardson), pp. 243–299. Applied Science Publishers.

LAPLACE, P. S. 1805 Theory of capillary attractions. Supplement to the *Tenth Book of Celestial Mechanics* (translated and annotated by N. Bowditch, 1839). Reprinted by Chelsea, New York, 1966.

LUTHER, L. C. 1986 Garnet melt viscosity, surface tension and drainage. *J. Cryst. Growth* **75**, 401–407.

MACKENZIE, J. D. 1956 The viscosity, molar volume and electric conductivity of liquid boron trioxide. *Trans. Faraday Soc.* **52**, 1564–1568.

MASON, G. 1970 An experimental determination of the stable length of cylindrical liquid bridges. *J. Colloid Interface Sci.* **32**, 172–176.

MELROSE, J. C. 1966 Model calculations for capillary condensation. *AIChE J.* **12**, 986–994.

MESEGUER, J. 1983 The breaking of axisymmetric slender liquid bridges. *J. Fluid Mech.* **130**, 123–151.

MOLLOT, D. J., TSAMOPOULOS, J. A., CHEN, T.-Y. & ASHGRIZ, N. 1993 Nonlinear dynamics of capillary bridges: experiments. *J. Fluid Mech.* **255**, 411–435.

PADDAY, J. F. 1971 The profiles of axially symmetric menisci. *Phil. Trans. R. Soc. Lond.* A **269**, 265–293.

PLATEAU, J. A. F. 1863 Experimental and theoretical researchers on the figures of equilibrium of a liquid mass withdrawn from the action of gravity. Translated in *Ann. Rep. Smithsonian Inst.*, pp. 207–285.

POSLINSKI, A. J. & TSAMOPOULOS, J. A. 1991 Inflation dynamics of fluid annular menisci inside a mold cavity – I. Deformation driven by small gas pressures. *Chem. Engng Sci.* **46**, 215–232.

PREISER, F., SCHWABE, D. & SCHARMANN, A. 1983 Steady and oscillatory thermocapillary convection in liquid columns with a free cylindrical surface, *J. Fluid Mech.* **126**, 545–567.

RAYLEIGH, LORD 1879 On the instability of jets. *Proc. Lond. Math. Soc.* **10**, 4–13.

RIVAS, D. & MESEGUER, J. 1984 One-dimensional self-similar solution of the dynamics of axisymmetric slender liquid bridges. *J. Fluid Mech.* **138**, 417–429.

SANZ, A. 1985 The influence of the outer bath in the dynamics of axisymmetric liquid bridges. *J. Fluid Mech.* **156**, 101–140.

THOMAS, P. D. & BROWN, R. A. 1987 LU decomposition of matrices with augmented dense constraints. *Intl J. Numer. Meth. Engng* **24**, 1451–1459.

TSAMOPOULOS, J. A. & BROWN, R. A. 1983 Nonlinear oscillations of inviscid drops and bubbles. *J. Fluid Mech.* **127**, 519–537.

TSAMOPOULOS, J. A. & BROWN, R. A. 1984 Resonant oscillations of inviscid charged drops. *J. Fluid Mech.* **147**, 373–395.

TSAMOPOULOS, J. A., CHEN, T.-Y. & BORKAR, A. 1992 Viscous oscillations of capillary bridges. *J. Fluid Mech.* **235**, 579–609.

TSAMOPOULOS, J. A., POSLINSKI, A. J. & RYAN, M. E. 1988 Equilibrium shapes and stability of captive annular menisci. *J. Fluid Mech.* **197**, 523–549.

YOUNG, T. 1805 Essay on the cohesion of fluids. *Phil. Trans. R. Soc. Lond.* A **306**, 347–370.

ZASADZINSKI, J. N., SWEENEY, J. B., DAVIS, H. T. & SCRIVEN, L. E. 1987 Finite element calculations of fluid menisci and thin-films in a model porous media. *J. Colloid Interface Sci.* **119**, 108–116.